

1 **Molecular chaperone ability to inhibit amyloid-derived neurotoxicity, but not**  
2 **amorphous protein aggregation, depends on a conserved pH-sensitive Asp residue**

3  
4 Gefei Chen<sup>1\*</sup>, Yuniesky Andrade-Talavera<sup>2#</sup>, Xueying Zhong<sup>3#</sup>, Sameer Hassan<sup>1#</sup>, Henrik  
5 Biverstal<sup>1,4</sup>, Helen Poska<sup>1,5</sup>, Axel Abelein<sup>1</sup>, Axel Leppert<sup>1</sup>, Nina Kronqvist<sup>1</sup>, Anna Rising<sup>1</sup>,  
6 Hans Hebert<sup>3</sup>, Philip J.B. Koeck<sup>3</sup>, André Fisahn<sup>2</sup>, Jan Johansson<sup>1</sup>

7  
8 <sup>1</sup>Department of Biosciences and Nutrition, Karolinska Institutet, 141 52 Huddinge, Sweden

9 <sup>2</sup>Department of Neurobiology, Care Sciences and Society, Center for Alzheimer Research,  
10 Division of Neurogeriatrics, Neuronal Oscillations Laboratory, Karolinska Institutet, 171 77  
11 Stockholm, Sweden

12 <sup>3</sup>School of Engineering Sciences in Chemistry, Biotechnology and Health, Department of  
13 Biomedical Engineering and Health Systems, KTH Royal Institute of Technology, 141 52  
14 Huddinge, Sweden

15 <sup>4</sup>Department of Physical Organic Chemistry, Latvian Institute of Organic Synthesis, Riga  
16 LV-1006, Latvia

17 <sup>5</sup>School of Natural Sciences and Health, Tallinn University, Tallinn, Estonia

18 # These authors contributed equally.

19 \*Corresponding author, E-mail: gefei.chen@ki.se

20  
21  
22  
23  
24  
25  
26  
27  
28  
29  
30  
31  
32  
33  
34

35 **Abstract**

36 Proteins can self-assemble into amyloid fibrils or amorphous aggregates and thereby cause  
37 disease. Molecular chaperones can prevent both these types of protein aggregation, but the  
38 respective mechanisms are not fully understood. The BRICHOS domain constitutes a  
39 disease-associated small heat shock protein-like chaperone family, with activities against  
40 both amyloid toxicity and amorphous protein aggregation. Here, we show that the activity of  
41 two BRICHOS domain families against Alzheimer's disease associated amyloid- $\beta$   
42 neurotoxicity to mouse hippocampi *in vitro* depends on a conserved aspartate residue, while  
43 the ability to suppress amorphous protein aggregation is unchanged by Asp to Asn mutations.  
44 The conserved Asp in its ionized state promotes structural flexibility of the BRICHOS  
45 domain and has a pKa value between pH 6.0–7.0, suggesting that chaperone effects against  
46 amyloid toxicity can be affected by physiological pH variations. Finally, the Asp is  
47 evolutionarily highly conserved in >3000 analysed BRICHOS domains but is replaced by  
48 Asn in some BRICHOS families and animal species, indicating independent evolution of  
49 molecular chaperone activities against amyloid fibril formation and non-fibrillar amorphous  
50 protein aggregation.

51

52

53 **Introduction**

54 Proteins and peptides can self-assemble into highly ordered fibrillar structures as well as into  
55 smaller oligomers with less well-defined structures but apparently stronger ability to cause  
56 toxicity to cells. These phenomena are linked to so-called amyloid diseases, which  
57 encompass about forty severe human diseases including interstitial lung disease (ILD) and  
58 Alzheimer's disease (AD)(1, 2). A multitude of proteins have been shown to form amyloid  
59 fibrils *in vitro* and generate cytotoxic species, yet they are not found in association with  
60 disease, which suggest that efficient chaperoning and/or other defence systems are in place(3,  
61 4). Molecular chaperones prevent protein aggregation and cytotoxicity(5), and  
62 chaperonopathy might occur during *e.g.* ageing and by genetic mutations, leading to protein  
63 misfolding disorders(6-8). However, no clear correlation between the clinical phenotype and  
64 the severity of anti-aggregation defects of disease-causing molecular chaperone mutations  
65 has been shown for *e.g.*, DNAJB6b and HSPB1(9, 10).

66

67 Many exceptionally amyloidogenic polypeptides are expressed as proproteins which are  
68 subjected to proteolytic cleavage to release the amyloidogenic fragments(11-13). Some of  
69 these proproteins contain the small heat shock protein (sHSP)-like domain BRICHOS,  
70 initially found in integral membrane protein 2B (also called **Bri2**), **Chondromodulin-1** and  
71 prosurfactant protein C (proSP-C)(14, 15). The BRICHOS domain is supposed to promote  
72 the correct folding and prevent amyloid formation of the amyloid-prone region of its  
73 proprotein during biosynthesis(16-18), and is released by proteolysis(19-21). Mutations in the  
74 BRICHOS domain or in the proproteins are associated with different protein misfolding and  
75 amyloid diseases(16, 22, 23), but the underlying pathogenic mechanisms are largely  
76 unknown. The BRICHOS domain has been shown to have chaperone activities also in *trans*  
77 against amyloid fibril formation and toxicity of several peptides associated with human  
78 diseases(21, 24, 25) and has emerged as a model compound in studies of amyloid fibril  
79 formation(26-29). AD relevant amyloid- $\beta$  with 42 residues (A $\beta$ 42) forms amyloid fibrils via  
80 several microscopic nucleation steps (*i.e.*, primary nucleation, elongation, and secondary  
81 nucleation), whereby A $\beta$ 42 oligomers are generated, which are supposed to be the main toxic  
82 species that drive AD development(27). The recombinant human (rh) BRICHOS domain  
83 from proSP-C is an efficient inhibitor of amyloid toxicity of A $\beta$ 42 *in vitro* in mouse  
84 hippocampal slice preparations, reducing the generation of toxic A $\beta$ 42 oligomers, but it is not  
85 very competent to reduce the overall amyloid fibril formation rate(24, 27). *In vivo* proSP-C

86 BRICHOS has shown positive effects on locomotion and longevity when co-expressed with  
87 A $\beta$ 42 in a *Drosophila* fruit fly model(30, 31). The rh Bri2 BRICHOS, on the other hand, is  
88 efficient in inhibiting both A $\beta$ 42 amyloid fibril formation rate and toxicity by assembling into  
89 differently sized species, of which monomers potently prevent neuronal network toxicity of  
90 A $\beta$ 42, dimers strongly suppress A $\beta$  fibril formation and large oligomers inhibit non-fibrillar  
91 protein aggregation(24, 30, 32, 33). Interestingly, for the BRICHOS domains studied so far,  
92 the ability to suppress amorphous protein aggregation, the canonical molecular chaperone  
93 function, is not coupled to the ability to prevent amyloid fibril formation or toxicity. ProSP-C  
94 BRICHOS essentially lacks activity against amorphous protein aggregation, while Bri2 and  
95 Bri3 BRICHOS inhibit both fibrillar and non-fibrillar aggregation(32, 34). We could recently  
96 explain the basis for this discrepancy by showing that the canonical chaperone activity to  
97 suppress amorphous protein aggregation is determined by specific loop segments in  
98 BRICHOS, while the activity against amyloid formation is independent of these segments  
99 (Chen et al, submitted for publication).

100  
101 Recently, a Bri2 BRICHOS mutant (R221E), designed to stabilize the monomeric  
102 conformation, showed great potential in the prevention and treatment of AD by alleviating  
103 A $\beta$ 42 neurotoxicity rather than its overall fibrillization rate(33). A corresponding mutation in  
104 proSP-C BRICHOS (T187R) likewise generates monomers that bind to the smallest  
105 emerging A $\beta$ 42 oligomers(28). Surprisingly, T187N mutation of human proSP-C BRICHOS  
106 leads to ILD with amyloid deposits, while the T187R mutant is more efficient *in vitro* than  
107 the wildtype against amyloid fibril formation(28, 35). Thus, understanding the molecular  
108 mechanisms that regulate BRICHOS chaperone activities are of interest from a basic science  
109 point of view and for the development of treatments against amyloid diseases. In the  
110 BRICHOS superfamily, the secondary structure elements are highly conserved but the amino  
111 acid sequence conservation is low, and only one aspartic acid residue (Asp, D) and two  
112 cysteine residues that form a disulphide bridge were previously found to be strictly conserved,  
113 from analyses of a rather small number of sequences(14, 33). The physiological function of  
114 this Asp is unknown, yet two mutations of D105 in human proSP-C BRICHOS are linked to  
115 ILD(16, 20, 36). Herein, we analysed all BRICHOS proproteins deposited in sequence  
116 databases and studied experimentally how BRICHOS capacities against amyloid formation  
117 and toxicity, as well as non-fibrillar protein aggregation is affected by the conserved Asp. We  
118 found that the evolutionarily conserved Asp is replaced by Asn in some BRICHOS families, is

119 protonated at physiological pH and is essential for preventing amyloid toxicity but not  
120 amorphous aggregation.

121

## 122 **Results**

### 123 **Evolutionary analyses of BRICHOS domains**

124 As substantially more BRICHOS containing proteins have been described from genome  
125 sequencing since the initial analyses were performed, we undertook detailed phylogenetic  
126 and sequence analyses of all so far reported BRICHOS containing proteins. Amino acid  
127 sequences of 3 355 BRICHOS precursors were extracted from the SMART database,  
128 covering a broad distribution of 537 different metazoan species from worms to humans,  
129 grouped into eleven phyla (**Fig. 1a and b**). After sorting out repetitive and incomplete  
130 sequences, 2 019 BRICHOS sequences from 1 968 precursors were retained for further  
131 analysis. These BRICHOS domains were separated into thirteen groups, which include  
132 eleven previously known families (integral membrane protein 2A (ITM2A), ITM2B (also  
133 called Bri2), ITM2C (also called Bri3), group I, gastrokine-1 (GKN1), GKN2, GKN3,  
134 tenomodulin (TNMD), chondromodulin (CNMD, previously called LECTI), proSP-C,  
135 BRICHOS containing domain 5 (BRICD5) and two novel families (group II and  
136 antimicrobial peptide (AMP)) (**Fig. 1c centre and inner ring, supplementary Fig. 1**). The  
137 BRICHOS domains in the AMP group were recently found in marine animals to help  
138 antimicrobial peptides to fold correctly(37-39), while the BRICHOS domains in group II  
139 have unknown functions.

140

141 Interestingly, analyses of the 1 968 precursors of the 2 019 BRICHOS domains showed that  
142 there are a few BRICHOS containing proproteins that contain multiple BRICHOS domains  
143 along with their corresponding amyloid-prone regions (**Fig. 1d and e, Supplementary Fig.**  
144 **2**). Multiple BRICHOS domains were found in GKN1, proSP-C, CNMD and group II  
145 families (**Fig. 1c outer ring**). In total 99% (1948 out of 1968) of BRICHOS precursors  
146 contain a single BRICHOS domain, while 1% possess multiple BRICHOS domains (up to  
147 nineteen BRICHOS domains were found in one precursor) (**Fig. 1f, Supplementary Fig. 2**).  
148 The multiple BRICHOS domains within one precursor showed pairwise identities from 48%  
149 to 97% (**Supplementary Table 1**), indicating that they arose by duplications. Alignment of  
150 all compiled BRICHOS amino acid sequences showed that the Asp residue, which previously  
151 was found to be strictly conserved, did not show 100% conservation in neither the single nor  
152 the multiple BRICHOS domains (**Fig. 2a and b, Supplementary Fig. 3 and 4**). In the single

153 BRICHOS domains, 97% (1853 out of 1908) contain the conserved Asp, while 2.7% have  
154 Asn, and the remaining 0.3% are distributed between Glu (E) and Ser (S) (**Fig. 2c**). Within  
155 the multiple BRICHOS domains, the percentage having Asp was markedly decreased to 31%,  
156 while instead 68% contain Asn, and one example with Glu was found (**Fig. 2d**). In the cases  
157 of multiple BRICHOS containing proproteins, 85% have either Asp or Asn, and 15% utilize  
158 both Asp and Asn (or Glu) (**Fig. 2e, Supplementary Fig. 2**). Among the BRICHOS domains  
159 derived from single BRICHOS precursors, the ones having Asn were found in GKN1, GKN3,  
160 ITM2A, and proSP-C BRICHOS families (**Fig. 2a and f**), and were mainly found in birds  
161 (Aves, 81%) with only 19% from Mammalia (**Fig. 2f**). An interesting observation is that bird  
162 surfactant lacks SP-C(40), so the BRICHOS containing proSP-C from birds likely have  
163 evolved other functions than to generate SP-C. Surprisingly, all the non-Asp BRICHOS  
164 domains from the multiple BRICHOS precursors were found in the GKN1 family and are all  
165 from birds (**Fig. 2g**).

166

### 167 **Ionization and protonation of the Aspartate within a physiological pH range**

168 The results from the evolutionary studies prompted us to mutate the conserved Asp to Asn in  
169 human BRICHOS domains from proSP-C (Asp105) and Bri2 (Asp148), which are the most  
170 studied BRICHOS domains.

171

172 Size exclusion chromatography (SEC) showed that both wildtype and D105N rh proSP-C  
173 BRICHOS adopt trimeric conformation, but the mutant formed more dimers and less  
174 monomers than the wildtype protein (**Supplementary Fig. 5a**). Circular dichroism (CD)  
175 spectroscopy showed rh proSP-C BRICHOS D105N is overall more structured than the  
176 wildtype at neutral pH as judged from a shift from the minimum around 202 nm to around  
177 207 nm, while at acidic pH the CD spectra are virtually identical (**Supplementary Fig. 5b**  
178 and **c**). To see whether wildtype rh proSP-C BRICHOS titrates with an elevated pKa value  
179 (compared to pKa of about 4.5 for free Asp in solution), we followed the CD signal at 204  
180 nm of rh proSP-C BRICHOS between pH 7.0 and 5.0, which gave an apparent pKa value of  
181 the transition of about 6.1 (**Fig. 2h, Supplementary Fig. 5b**). Notably, the CD spectra of rh  
182 proSP-C BRICHOS D105N did not shift substantially between pH 5.5 and 8.0 (**Fig. 2h**,  
183 **Supplementary Fig. 5c**), suggesting that protonation of D105 is a main determinant of the  
184 observed conformational shift, and it may be the sole titrating residue in this pH range. To  
185 confirm the pH-dependent conformational changes, we ran NMR spectroscopy on wildtype  
186 rh proSP-C BRICHOS labelled with <sup>15</sup>N, <sup>13</sup>C and <sup>2</sup>H at different pHs. The comparison of the

187  $^{15}\text{N}$ -HSQC spectra at pH 5.5 and 7.2 showed clear chemical shift changes, supporting that rh  
188 proSP-C BRICHOS undergoes structural changes in this pH range (**Supplementary Fig. 5d**).  
189

190 Rh wildtype NT\*-Bri2 BRICHOS(33) and rh NT\*-Bri2 BRICHOS D148N showed similar  
191 elution profiles on SEC (**Supplementary Fig. 5e**). After removal of the NT\* solubility tag, rh  
192 Bri2 BRICHOS D148N formed similar disulphide-dependent assembly states as the wildtype  
193 protein (**Supplementary Fig. 5f-h**). However, the rh Bri2 BRICHOS D148N dimers are  
194 exclusively disulphide-linked (**Supplementary Fig. 5h, Figure 5-figure supplement 5-**  
195 **source data**), while the wildtype dimers are a mixture of disulphide-linked and non-covalent  
196 species(32). Moreover, rh Bri2 BRICHOS D148N generated from the rh NT\*-Bri2  
197 BRICHOS D148N monomer fraction did not elute on SEC as a monomer but as a dimer,  
198 while both the corresponding oligomers and dimers shared similar elution profiles as the  
199 corresponding wildtype states (**Supplementary Fig. 5f and g**). This indicates that the rh Bri2  
200 BRICHOS D148N monomers are not stable but form non-covalent dimers. Rh Bri2  
201 BRICHOS D148N oligomers and dimers shared identical CD spectra as the corresponding  
202 wildtype species, whereas the initially monomeric rh Bri2 BRICHOS D148N showed a  
203 somewhat different CD spectrum compared to the wildtype monomers (**Supplementary Fig.**  
204 **5i-l**), but which can be superimposed on the wildtype dimer spectrum (**Supplementary Fig.**  
205 **5l**). This suggests the rh Bri2 BRICHOS D148N monomer mainly assembles into a dimer at  
206 the concentration used for CD spectroscopy. As analysed by SEC, at one  $\mu\text{mol L}^{-1}$ , rh  
207 wildtype Bri2 BRICHOS monomer migrated solely as a monomer, and with increasing  
208 concentration, dimers were progressively formed (**Supplementary Fig. 6a, Supplementary**  
209 **Fig. 7**). However, an equilibrium between dimers and monomers were seen even at 200  $\mu\text{mol}$   
210  $\text{L}^{-1}$  (**Supplementary Fig. 6a, Supplementary Fig. 7e**). In contrast, already at low  
211 concentrations (0.5  $\mu\text{mol L}^{-1}$ ) rh Bri2 BRICHOS D148N showed an equilibrium between  
212 dimers and monomers, approximately at a ratio of 1:1 (**Supplementary Fig. 6b,**  
213 **Supplementary Fig. 8a**). With progressively increased concentrations rh Bri2 BRICHOS  
214 D148N monomers transformed to dimers and at 100  $\mu\text{mol L}^{-1}$  all proteins migrated as dimers  
215 (**Supplementary Fig. 6b, Supplementary Fig. 8f**). To get further details on how rh Bri2  
216 BRICHOS undergoes monomer-dimer transition, we analysed SEC profiles at different pHs.  
217 At pH 7.0 to 8.0 both rh Bri2 BRICHOS D148N and wildtype monomers showed similar  
218 elution volumes (**Supplementary Fig. 6c and d**). However, at pH 6.0 rh wildtype Bri2  
219 BRICHOS elutes as a dimer, whereas the D148N mutant did not show any significant  
220 difference compared to the elution volume at pH 7.0 and 8.0 (**Supplementary Fig. 6c and d**).

221 This suggests that at pH between 7.0 and 6.0 Asp148 can be protonated with subsequent shift  
222 of the dimer-monomer equilibrium towards dimers. To corroborate the supposition that  
223 Asp148 titrates between pH 6.0 and 7.0 we turned to a rh Bri2 BRICHOS variant with  
224 Thr206 replaced by Trp (T206W) that displayed an identical oligomerization profile as the rh  
225 wildtype Bri2 BRICHOS (**Supplementary Fig. 9a**), but a different Trp fluorescence profile  
226 in the monomeric state compared to the dimeric state (**Supplementary Fig. 9b**). In  
227 agreement with SEC data, titration of the rh Bri2 BRICHOS Trp mutant showed a  
228 fluorescence evolution (monomer/dimer transition) with a pKa of 6.7 (**Fig. 2i**,  
229 **Supplementary Fig. 9c**).

230

231 These observations indicate that the D148N mutation in rh Bri2 BRICHOS promotes  
232 monomer to dimer conversion, and mimics pH-induced dimerization of the wildtype  
233 monomers with an apparent pKa of 6.7, but it does not significantly change the assembly of  
234 dimers into larger oligomers. Analogously, the mutation D105N in rh proSP-C BRICHOS  
235 results in a more compact conformation and possibly more complete assembly into trimers,  
236 and the wildtype rh proSP-C BRICHOS conformational shift by CD titrates with an apparent  
237 pKa of 6.1.

238

### 239 **The conserved Asp of BRICHOS is essential for the capacity to prevent A $\beta$ 42-induced 240 neurotoxicity**

241 To investigate the importance for the ability to alleviate amyloid-induced neurotoxicity, we  
242 tested the efficacies of Asp to Asn mutated vs. wildtype BRICHOS in preventing A $\beta$ 42-  
243 induced reduction of  $\gamma$  oscillations in mouse hippocampal slices.  $\gamma$  oscillations correlate with  
244 learning, memory, cognition and other higher processes in the brain(41, 42) and progressive  
245 cognitive decline observed in AD goes hand-in-hand with a progressive decrease of  $\gamma$   
246 oscillations(43-45). The BRICHOS domains from human proSP-C and Bri2 can efficiently  
247 prevent A $\beta$ 42-induced decline in hippocampal  $\gamma$  oscillations(27, 30, 32, 33, 46). In addition,  
248 rh Bri2 BRICHOS rescues  $\gamma$  oscillations and neuronal network dynamics from A $\beta$ 42-induced  
249 impairment at hippocampal CA3 area *ex vivo*(47). We recorded  $\gamma$  oscillations in hippocampal  
250 slices from wildtype C57BL/6 mice preincubated for 15 min either with 50 nmol L<sup>-1</sup> A $\beta$ 42  
251 alone, or co-incubated with 100 nmol L<sup>-1</sup> rh wildtype or D105N proSP-C BRICHOS (**Fig.**  
252 **3a**).  $\gamma$  oscillations were elicited by application of 100 nmol L<sup>-1</sup> kainic acid (KA) and allowed  
253 to stabilize for 30 min prior to any recordings. As previously observed(27, 30, 46), 100 nmol

254  $\text{L}^{-1}$  wildtype proSP-C BRICHOS prevented  $\text{A}\beta 42$ -induced degradation of  $\gamma$  oscillations,  
255 which were remained at control levels (**Fig. 3b and c**, control:  $1.7 \pm 0.16 \times 10^{-8} \text{ V}^2 \text{ Hz}^{-1}$ ,  $n=$   
256 20;  $\text{A}\beta 42$ :  $0.34 \pm 0.06 \times 10^{-8} \text{ V}^2 \text{ Hz}^{-1}$ ,  $n= 14$ ,  $p < 0.0001$  vs. control; + rh wildtype proSP-C  
257 BRICHOS:  $1.41 \pm 0.24 \times 10^{-8} \text{ V}^2 \text{ Hz}^{-1}$ ,  $n= 9$ ) (**Supplementary Table 2, Figure 3-source**  
258 **data**). By contrast, rh proSP-C BRICHOS D105N showed a complete loss of the preventative  
259 efficacy at the same concentration (**Fig. 3b and c**, rh proSP-C BRICHOS D105N:  $0.36 \pm$   
260  $0.09 \times 10^{-8} \text{ V}^2 \text{ Hz}^{-1}$ ,  $n= 9$ ,  $p= 0.0202$  vs. rh wildtype proSP-C BRICHOS,  $p= 0.0002$  vs.  
261 control,  $p > 0.9999$  vs.  $\text{A}\beta 42$ ) (**Supplementary Table 2, Figure 3-source data**). We have  
262 previously observed that the rh Bri2 BRICHOS monomer is most efficient at preventing  
263  $\text{A}\beta 42$  induced degradation of  $\gamma$  oscillations(32, 33). We therefore tested whether the D148N  
264 mutation could affect the efficacy of rh Bri2 BRICHOS monomers. Rh Bri2 BRICHOS  
265 D148N monomers ( $50 \text{ nmol L}^{-1}$ ) showed reduced tendency of potency to prevent  $\text{A}\beta 42$ -  
266 induced neurotoxicity compared to wildtype monomers ( $50 \text{ nmol L}^{-1}$ ), but did not completely  
267 lose preventative efficacy, as observed for rh proSP-C BRICHOS D105N (**Fig. 3d and e**, rh  
268 wildtype Bri2 BRICHOS monomers:  $1.35 \pm 0.29 \times 10^{-8} \text{ V}^2 \text{ Hz}^{-1}$ ,  $n= 8$ ,  $p > 0.9999$  vs. control;  
269 rh Bri2-BRICHOS D148N monomers:  $0.7 \pm 0.14 \times 10^{-8} \text{ V}^2 \text{ Hz}^{-1}$ ,  $n= 11$ ,  $p= 0.3494$  vs. rh  
270 wildtype Bri2 BRICHOS monomers,  $p= 0.003$  vs. control,  $p= 0.6991$  vs.  $\text{A}\beta 42$ )  
271 (**Supplementary Table 2, Figure 3-source data**). These results suggest that the  
272 phylogenetically conserved Aspartate plays a crucial role in maintaining the anti-amyloid  
273 neurotoxicity capacity of BRICHOS.

274

### 275 **The conserved Asp of BRICHOS is not important for canonical chaperone activity** 276 **against amorphous protein aggregation or Bri2 BRICHOS oligomer structure**

277 The rh wildtype Bri2 BRICHOS oligomers are efficient molecular chaperones against non-  
278 fibrillar protein aggregation, evaluated by thermo-induced citrate synthase aggregation as a  
279 model(32). This was found to be true also for the rh Bri2 BRICHOS D148N oligomers (**Fig.**  
280 **5a and b**). Similarly, the D105N mutation did not show any effects on the capacity of rh  
281 proSP-C BRICHOS trimer against amorphous protein aggregation, *i.e.*, both the wildtype and  
282 D105N mutant are essentially inactive as regards canonical chaperone activity  
283 (**Supplementary Fig. 10a**). This shows a strong difference in the importance of the  
284 conserved Asp in BRICHOS for activity against amyloid toxicity compared to activity  
285 against amorphous protein aggregation.

286

287 Although the D148N mutation changed the balance between monomers and dimers of rh Bri2  
288 BRICHOS, the mutant still formed large oligomeric species with a similar secondary  
289 structure as wildtype oligomers (**Supplementary Fig. 5e, g and i**). We isolated rh Bri2  
290 BRICHOS D148N oligomers by SEC, recorded transmission electron microscopy (TEM)  
291 micrographs and calculated 3D reconstructions (**Fig. 4c and d, Supplementary Fig. 10b and**  
292 **c, Figure 4-source data**). The micrographs and 2D class averages revealed mostly  
293 homogenous large assemblies with two-fold symmetry (**Fig. 4c**). As a result, an EM map was  
294 reconstructed with D2 symmetry from 10 223 manually extracted single particles (**Fig. 4d,**  
295 **Figure 4-source data**). The rh Bri2 BRICHOS D148N oligomer 3D model and the one from  
296 the wildtype oligomers(32) overlap and share overall similar shape and volume (**Fig. 4e,**  
297 **Figure 4-source data**), suggesting that the overall structure of the large Bri2 BRICHOS  
298 oligomers is not noticeably changed when Asp148 is mutated to Asn.

299

300 **Molecular mechanisms underlying the importance of the conserved Asp of BRICHOS**  
301 **for**

302 **ability to suppress A $\beta$ 42 neurotoxicity**

303 To further explore whether the diminished BRICHOS capacity against amyloid neurotoxicity  
304 caused by Asp to Asn mutation correlates with the activity of suppressing macroscopic  
305 amyloid fibril formation, we used thioflavin T (ThT)(48) fluorescence to monitor the kinetics  
306 of A $\beta$ 42 fibril formation in the absence and presence of different concentrations of rh Bri2 or  
307 proSP-C BRICHOS (**Fig. 5**). Both the rh wildtype proSP-C BRICHOS and the D105N  
308 mutant showed dose-dependent progressive reduction of A $\beta$ 42 fibril formation at  
309 stoichiometric concentrations, and the aggregation kinetics follows a typical sigmoidal  
310 behavior (**Fig. 5a and d-f, Supplementary Fig. 11a-c**). The A $\beta$ 42 fibrillization half time,  
311  $\tau_{1/2}$ , increases with increasing rh proSP-C BRICHOS concentration (**Fig. 5b**), while the  
312 maximum rate of A $\beta$ 42 aggregation,  $r_{max}$ , shows a mono-exponential decline (**Fig. 5c**).  
313 Interestingly, rh proSP-C BRICHOS D105N showed remarkably improved inhibition on  
314 A $\beta$ 42 fibril formation compared to the wildtype, manifested with both  $\tau_{1/2}$  and  $r_{max}$  (**Fig. 5a-**  
315 **c**), which is opposite compared to the effects on the capacity to prevent A $\beta$ 42-induced  
316 neurotoxicity (**Fig. 3**). On the other hand, similarly, the rh wildtype Bri2 BRICHOS  
317 monomers showed similar effects on  $\tau_{1/2}$  and  $r_{max}$  of A $\beta$ 42 fibrillization as reported (**Fig. 5g-**  
318 **i**)(32). The rh Bri2 BRICHOS D148N oligomers, dimers and monomers also presented dose-  
319 dependent inhibition on A $\beta$ 42 fibril formation with typical sigmoidal behavior (**Fig. 5g-i**,

320 **Supplementary Fig. 12).** Along the same lines, compared to wildtype monomers, the D148N  
321 monomers were significantly more efficient in inhibiting A $\beta$ 42 fibril formation (**Fig. 5g–i**),  
322 suggesting the Asp to Asn mutation pronouncedly enhances BRICHOS activity against  
323 overall fibril formation. The D148N monomers and dimers showed very similar inhibitory  
324 effects on A $\beta$ 42 fibrillization (**Supplementary Fig. 12a and b**), which likely can be  
325 explained by that D148N monomers and dimers are in equilibrium (**Supplementary Fig. 6b**  
326 **and 8**).

327

328 To find out the molecular mechanisms underlying how the Asp to Asn mutation decreases  
329 BRICHOS capacity against A $\beta$ 42 neurotoxicity but enhances its inhibitory activity against  
330 overall A $\beta$ 42 fibril formation, we investigated the effects of both rh wildtype BRICHOS and  
331 the corresponding Asp to Asn mutants on A $\beta$ 42 amyloid fibril formation and related  
332 microscopic events. A $\beta$ 42 fibrillization kinetics are described by a set of microscopic rate  
333 constants, *i.e.*, primary ( $k_n$ ) and surface-catalyzed secondary nucleation ( $k_2$ ) as well as  
334 elongation ( $k_+$ )(49), and perturbations of the individual microscopic rates are most relevant  
335 since their relative contributions determine the generation of nucleation units, which might be  
336 linked to the neurotoxic A $\beta$ 42 oligomeric species(27, 50). To evaluate the effects on  
337 individual microscopic processes, we performed global fits of the kinetics data sets at  
338 constant A $\beta$ 42 and different BRICHOS concentrations for both rh wildtype proSP-C and the  
339 D105N mutant, where the fits were constrained such that only one single rate constant, *i.e.*,  $k_n$ ,  
340  $k_2$  or  $k_+$ , is the sole fitting parameter (**Fig. 5d-f, Supplementary Fig. 11a–c**). As previously  
341 described(27), the rh wildtype proSP-C BRICHOS mainly interfered with the secondary  
342 nucleation, indicated by the perfect fits when  $k_2$  was the sole global fitting rate constant  
343 (**Supplementary Fig. 11a–c**). Also, the secondary nucleation rate  $k_2$  as the sole fitting  
344 parameter gave the best fits for the A $\beta$ 42 fibrillization kinetics with rh proSP-C BRICHOS  
345 D105N (**Fig. 5d-e**), but with worse quality compared to the wildtype, especially for the start  
346 of the aggregation traces. This suggests that a complex microscopic mechanism is present,  
347 which might also include fibril-end elongation ( $k_+$ ) and/or primary nucleation ( $k_n$ ) in addition  
348 to secondary nucleation ( $k_2$ ). To further study whether the fibril-end elongation process or the  
349 primary nucleation are affected in the presence of rh proSP-C BRICHOS D105N and  
350 wildtype forms, we determined aggregation kinetics in the presence of a high initial fibril  
351 seed concentration(49) and surface plasmon resonance (SPR) analysis. With seeding, the  
352 fibrillization traces typically follow a concave aggregation behavior (**Supplementary Fig.**

353 **11d and e)**, where the initial slope is directly proportional to the elongation rate  $k_+$ . These  
354 seeding experiments revealed that rh proSP-C BRICHOS D105N decreases the elongation in  
355 a dose-dependent manner, and already at low concentrations fibril-end elongation is  
356 noticeably retarded (**Fig. 5j, Supplementary Fig. 11e**). The rh wildtype proSP-C BRICHOS,  
357 in contrast, showed only slight effects on fibril-end elongation (**Fig. 5j, Supplementary Fig.**  
358 **11d**), which is further supported by immuno-transmission electron microscopy (immuno-EM)  
359 images where both rh proSP-C BRICHOS D105N and the wildtype attach along the A $\beta$ 42  
360 fibril surface, however, the fibril ends are apparently mainly blocked by the D105N mutant  
361 (**Fig. 5k**). Additionally, SPR analyses of A $\beta$ 42 monomers immobilized on a sensor chip  
362 indicated that rh wildtype proSP-C BRICHOS showed weak binding to the immobilized  
363 A $\beta$ 42 monomers in line with previous reports(27, 28). The D105N mutation significantly  
364 enhanced the BRICHOS-A $\beta$ 42 monomer interactions (**Supplementary Fig. 11f**) with an  
365 apparent affinity value  $K_D$  around 5  $\mu\text{mol L}^{-1}$  (**Fig. 5l**) from global kinetics fits, and under  
366 steady-state conditions a  $K_D$  value of around 25  $\mu\text{mol L}^{-1}$  was obtained (**Supplementary Fig.**  
367 **11g**). Interfering with primary nucleation ( $k_n$ ) delays A $\beta$ 42 fibril formation without changing  
368 the total number of oligomers generated, suppressing the secondary nucleation ( $k_2$ ) efficiently  
369 prevents the generation of oligomers, while blocking elongation ( $k_+$ ) significantly increases  
370 the number of oligomers formed(27). Of relevance for the results on A $\beta$ 42 neurotoxicity of  
371 wildtype vs D105N proSP-C BRICHOS (**Fig. 3**), we found that in the presence of equimolar  
372 ratio of rh proSP-C BRICHOS D105N, the A $\beta$ 42 fibrillization reaction generated  
373 approximately 5.2 times more oligomers than from A $\beta$ 42 alone, by significantly suppressing  
374 the fibril end elongation process, while the wildtype only showed slight effects (**Fig. 5j**  
375 **insets**). These observations show that both rh proSP-C BRICHOS D105N and the wildtype  
376 protein reduce A $\beta$ 42 fibrillization by blocking the surface-catalyzed secondary nucleation,  
377 while fibril-end elongation and possibility primary nucleation are substantially affected only  
378 by the D105N mutant. These results offer a molecular explanation to the observed loss of  
379 inhibitory effects of the rh proSP-C BRICHOS mutant on neurotoxic A $\beta$ 42 oligomer  
380 generation.

381  
382 To further study the mechanism underlying the reshaped interference of BRICHOS with  
383 A $\beta$ 42 monomer and fibrils, we used the non-polar fluorescent dye bis-ANS to probe the  
384 exposure of hydrophobic areas. Bis-ANS shows a blue shift of the emission maximum and  
385 increased emission intensity upon binding to exposed hydrophobic protein surfaces, which

386 has been applied to rh wildtype Bri2 and proSP-C BRICHOS(32, 51, 52). When incubated  
387 with bis-ANS, rh wildtype proSP-C BRICHOS gave an increase of emission intensity  
388 compared to bis-ANS in buffer, and a blue shift of the emission maximum from about 520  
389 nm to 495 nm (**Supplementary Fig. 11h**). Notably, the blue shift and the intensity increase  
390 for the D105N mutant at pH 8.0 are more pronounced compared to the wildtype protein  
391 (**Supplementary Fig. 11h**), showing that D105N results in more exposed hydrophobic areas,  
392 which may be important for A $\beta$ 42 fibril-end binding(32, 33) and monomer binding.  
393 Interestingly, when incubating bisANS with rh wildtype proSP-C BRICHOS at pH 6.0 an  
394 identical fluorescence spectrum as for the D105N mutant at pH 8.0 was observed  
395 (**Supplementary Fig. 11h**), indicating that the D105N mutation gives similar effects as  
396 protonating Asp105. For Bri2 BRICHOS, dimers were found previously to be most efficient  
397 in preventing A $\beta$ 42 overall fibril formation compared to the monomers and oligomers, while  
398 the monomers are most potent in preventing A $\beta$ 42 induced disruption of neuronal network  
399 activity(32, 33). The microscopic mechanisms of rh Bri2 BRICHOS D148N species were  
400 similar to the wildtype species, both the secondary nucleation and elongation of A $\beta$ 42 were  
401 affected (**Supplementary Fig. 12c-k**). However, the equilibrium between monomer and  
402 dimer was modified by the Asp to Asn mutant towards the dimer (**Supplementary Fig. 6a**  
403 and b, **Supplementary Fig. 7 and 8**), thus reducing the monomer that is predominantly  
404 active against A $\beta$ 42-induced neurotoxicity but increasing the dimer fraction, which is most  
405 active against A $\beta$ 42 fibril formation.

406

## 407 **Discussion**

408 In this work, we show that the capacity of sHSP-like chaperone domain BRICHOS to inhibit  
409 amyloid-associated neurotoxicity is dependent on a phylogenetically conserved Asp, whereas  
410 the capacity to suppress non-fibrillar, amorphous protein aggregation is not affected by  
411 mutating this Asp to Asn. Moreover, conformational changes occur as a result of Asp to Asn  
412 mutations in both proSP-C and Bri2 BRICHOS, those changes can partly be mimicked by  
413 lowered pH and the conserved Asp titrates with an apparent pKa of about 6.5 in both  
414 BRICHOS domains studied.

415

416 The Asp residue studied herein is the only conserved non-Cys residue in all known  
417 BRICHOS domains and two mutations of this residue in human proSP-C BRICHOS (D105)  
418 are linked to ILD(16, 20, 36). Based on molecular dynamic simulation(16), monomeric

419 wildtype proSP-C BRICHOS and the D105N mutant behaved differently: only minor  
420 conformational changes were seen in the mutant, but several large-scale changes occurred in  
421 the wildtype at moderately elevated temperatures, which resulted in a more loosely folded  
422 structure. We can rationalize our results against this background (**Fig. 6a and b**). D105N  
423 mutation in rh proSP-C BRICHOS indeed results in a more ordered conformation and  
424 apparently more efficient trimer formation, while D148N mutation of rh Bri2 BRICHOS  
425 results in more readily transition of monomers to more compact dimers (**Supplementary Fig.**  
426 **5a and f**). Similar effects as observed in the mutants were seen for the wildtype proteins  
427 when pH was lowered to 6-7 (**Fig. 2h and i**). This suggests that a negatively charged Asp  
428 side-chain is necessary for maintaining a “loose” flexible state of the BRICHOS subunit and  
429 that protonation, or replacement with a neutral Asn, results in a more “compact” state that is  
430 prone to form oligomers. In the open conformation, BRICHOS is efficient in alleviating  
431 A $\beta$ 42 amyloid neurotoxicity, while the compact conformation is more potent against overall  
432 amyloid fibril formation but inefficient against amyloid induced neurotoxicity (**Fig. 6b**).  
433 Interestingly, in brains of AD patients the pH is lower than that in the brains of healthy  
434 individuals(53), and at low pH A $\beta$  can form fibrils more efficiently than at neutral pH(54).  
435

436 The crystal structure of rh proSP-C BRICHOS, the only available high-resolution structure of  
437 a BRICHOS domain, gives limited information about the local environment of the conserved  
438 Asp since electron density is lacking for the part N-terminally of the juxtaposed helix 2(16).  
439 However, an inspection of amino acid sequence alignments of BRICHOS domains from all  
440 families show that there is a well conserved carboxylate residue situated just upstream of  
441 helix 2 (**Supplementary Fig. 3**, positions 176-180), and its location close to the sidechain of  
442 the strictly conserved Asp may contribute to the apparently elevated pKa values of D105 and  
443 D148 now observed. The distant evolutionary relationship between Bri2 and proSP-C  
444 BRICHOS domains, with <20% sequence identities, makes it likely that the common effects  
445 now observed between them also apply to other BRICHOS domains that exhibit similar  
446 evolutionary distances. Therefore, an elevated pKa value of the only strictly conserved non-  
447 Cys residue, as now found for proSP-C and Bri2 BRICHOS, is probably relevant for a  
448 common function of all BRICHOS domains, which thus likely requires a maintained “loose”  
449 conformation. Our results indicate that such a hypothetical common function is likely to be  
450 related to prevention of amyloid toxicity rather than prevention of amorphous protein  
451 aggregation. So far, molecular chaperones or chaperone-like domains have not been much  
452 studied extensively as regards sensitivity to pH. One exception is clusterin, whose activity is

453 enhanced at mildly acidic pH, which appears to result from an increase in regions with  
454 solvent-exposed hydrophobicity, but independent of any major changes in secondary or  
455 tertiary structure(55). The phylogenetic analyses showed the presence of the BRICHOS  
456 domain in a broad array of proproteins and species. In some cases where multiple BRICHOS  
457 domains are found, the conserved Asp is preferentially replaced with Asn (**Fig. 1 and 2**).  
458 Considering the experimental results herein this may suggest that BRICHOS has adopted  
459 different types of molecular chaperone activities during evolution.

460

461 Molecule chaperones are essential guards of all living cells, while the chaperoning  
462 abnormality may cause disease—chaperonopathy. The chaperoning capacities of BRICHOS  
463 domain against amyloid neurotoxicity and fibril formation can apparently be modulated by a  
464 conserved Asp in response to pH changes. In the human brain, pH decreases with aging(56),  
465 and also pH is significantly lower in patients than in healthy controls in different human brain  
466 disorders(53, 57). The observed phenomenon in this study suggests the possibility that  
467 microenvironmental changes may lead to human disease. The results here are based on *in*  
468 *vitro* and *ex vivo* experiments, and further *in vivo* work that focuses on the activities of  
469 BRICHOS and pH-mediated regulation can shed further light on this.

470

## 471 **Materials and Methods**

### 472 **Phylogenetic analysis of BRICHOS domain**

473 From the SMART database(58), 3 355 BRICHOS sequences were downloaded while the sole  
474 bacterial BRICHOS precursor (*Paeniclostridium sordellii* ATCC 9714) was not included.  
475 Incomplete sequences were filtered out, resulting in total of 3 190 sequences. Identical  
476 sequences were filtered by means of CD-HIT(59), with a threshold of 100% of sequence  
477 identity, which gave 3 093 amino acid sequences. The hidden markov model profile (HMM)  
478 of BRICHOS (PF04089) was extracted from PFAM database(60). The CD-HIT filtered  
479 BRICHOS protein sequences were then scanned against the HMM profile using HMMER  
480 software v3.3.2(61) with an E-value cut-off less than  $1.0 \times 10^{-5}$ . An in-house python script was  
481 written to filter out the significant BRICHOS proteins from the HMM result file and to  
482 extract the BRICHOS domain sequences (each BRICHOS amino acid sequence was extended  
483 six residues upstream from the BRICHOS domain starting position defined by PFAM).  
484 Further, BRICHOS domain sequences less than 68 aa were removed as one rodent BRICHOS  
485 domain is just 69 residues and still functional against amyloid fibril formation(62), which  
486 eventually generated 2 019 BRICHOS sequences. The multiple sequence alignment of the 2

487 019 BRICHOS domain sequences were created using MAFFT alignment server with the  
488 default settings(63), and the sequence logo was generated using Weblogo webserver(64).  
489 RAxML HPC(v8.2.10)(65) was employed for constructing the phylogenetic tree using the  
490 PROTGAMMAAUTO model with 100 times bootstrap iterations. The tree shown in this  
491 study was visualized using the Interactive Tree of Life (iTOL) server(66) and Geneious  
492 software. The taxonomy tree common for species that contain BRICHOS precursors were  
493 generated by NCBI Taxonomy  
494 (<https://www.ncbi.nlm.nih.gov/Taxonomy/CommonTree/wwwcmt.cgi>) and visualized by  
495 Geneious software.

496

#### 497 **Rh Bri2 BRICHOS and rh proSP-C BRICHOS wildtype and mutant preparation**

498 For generating rh Bri2 BRICHOS D148N, the amplification primers 5'-  
499 ATAGTGATCCTGCCAACATTGATAACTTTAACAAAGAAACTTACA-3' and 5'-  
500 TGTAAGTTCTTGTAAAGTTATGAACAATGTTGGCAGGATCACTAT-3' were  
501 synthesized. With the wildtype NT\*-Bri2 BRICHOS (corresponding to the solubility tag NT\*  
502 followed by Bri2 residues 113–231(32, 67)) plasmid as PCR template Bri2 BRICHOS  
503 D148N was obtained with QuikChange II XL Site-Directed Mutagenesis Kit (Agilent, US),  
504 and the DNA sequence was confirmed (GATC Bioteq, Germany). Similarly, the amino acid  
505 Thr at position 206 was mutated to Trp using KAPA HiFi HotStart ReadyMix PCR Kit (Kapa  
506 Biosystems, USA) together with the designed complementary primers (5'-  
507 CCTATCTGATTGAGCACATGGTTATTGGGATCGCATTGAAAAC-3' and 5'-  
508 GTTTCAATGCGATCCAAATAACCATGTGCTCATGAATCAGATAGG-3') and  
509 verified by sequencing (Eurofins Genomics). As described(32, 33) , the Bri2 BRICHOS  
510 variants were expressed in SHuffle T7 *E. coli* cells. Briefly, the cells were incubated at 30°C  
511 in LB medium with 15 µg mL<sup>-1</sup> kanamycin until an OD<sub>600 nm</sub> around 0.9. For overnight  
512 expression, the temperature was lowered to 20°C, and 0.5 mmol L<sup>-1</sup> (final concentration)  
513 isopropyl β-D-1-thiogalactopyranoside (IPTG) was added. The induced cells were harvested  
514 by centrifugation (4°C, 7 000 ×g) and the cell pellets were resuspended in 20 mmol L<sup>-1</sup> Tris  
515 pH 8.0. After 5 min sonication (2 s on, 2 s off, 65% power) on ice, the lysate was centrifuged  
516 (4°C, 24 000 ×g) for 30 min and the protein of interest was isolated with a Ni-NTA column.  
517 To remove the His<sub>6</sub>-NT\* part, the target proteins were cleaved with thrombin (1:1 000, w/w)  
518 at 4°C overnight and loaded over a second Ni-NTA column. Different species of rh Bri2  
519 BRICHOS variants were isolated and analysed by Superdex 200 PG, 200 GL or 75 PG

520 columns (GE Healthcare, UK) using an ÄKTA system (GE Healthcare, UK) with buffer of  
521 20 mmol L<sup>-1</sup> NaPi (Sodium Phosphate) with 0.2 mmol L<sup>-1</sup> EDTA at different pHs. For  
522 generating rh proSP-C BRICHOS D105N, the PCR primers 5'-  
523 CACTGGCCTCGTGGTGTATAACTACCAGCAGCTGCTGATCGC-3' and 5'-  
524 GCGATCAGCAGCTGCTGGTAGTTATACACCACGAGGCCAGTG -3' were synthesized.  
525 With the wildtype proSP-C BRICHOS (corresponding to the solubility tag thioredoxin  
526 followed by proSP-C residues 86–197(16)) plasmid as PCR template, proSP-C BRICHOS  
527 D105N was obtained with QuikChange II XL Site-Directed Mutagenesis Kit (Agilent, US),  
528 and the DNA sequence was confirmed (GATC Bioteq, Germany). The expression and  
529 purification were performed as described(16, 68). Briefly, both wildtype proSP-C BRICHOS  
530 and the D105N mutant were expressed in Origami 2 (DE3) pLysS *E. coli* cells. The cells  
531 were grown at 37°C in LB medium containing 100 µg mL<sup>-1</sup> ampicillin until an OD<sub>600 nm</sub>  
532 around 0.9. The temperature was lowered to 25°C and 0.5 mmol L<sup>-1</sup> (final concentration)  
533 IPTG was added for overnight expression. The cells were harvested by centrifugation at 7  
534 000 × g for 20 min, and the cell pellets were resuspended in 20 mmol L<sup>-1</sup> Tris pH 8.0. The  
535 protein was purified using Ni-NTA column and ion exchange chromatography (QFF, GE  
536 Healthcare). Thrombin (1:1 000, w/w) was used to remove the thioredoxin tag. The purified  
537 rh proSP-C BRICHOS variants were analysed by Superdex 200 GL columns (GE Healthcare,  
538 UK) using an ÄKTA system (GE Healthcare, UK). The BRICHOS mutants in this study  
539 were expressed and purified in parallel with their wildtype counterparts.

540

## 541 **NMR spectroscopy**

542 For the NMR experiments, gene fragment encoding human proSP-C BRICHOS was  
543 transformed into SHuffle T7 *E. coli* cells and was grown in LB with gradually increasing  
544 D<sub>2</sub>O content (25%, 50%, 75% and 100%). At 100% D<sub>2</sub>O, 1 mL LB was used to inoculate 100  
545 mL M9 in 100% D<sub>2</sub>O enriched with <sup>15</sup>N H<sub>4</sub>Cl and <sup>13</sup>C glucose, and was grown over night at  
546 31°C. After overnight incubation, the 100 mL was added to 900 mL M9 in D<sub>2</sub>O enriched  
547 with <sup>15</sup>N and <sup>13</sup>C and grown at 30°C until OD<sub>600 nm</sub> was around 0.8. The temperature was  
548 lowered to 20°C and 0.5 mmol L<sup>-1</sup> (final concentration) IPTG was added for overnight  
549 expression. The purification was performed as described above.

550

551 2D <sup>1</sup>H-<sup>15</sup>N TROSY-HSQC experiments were obtained at 37°C on Bruker 800 MHz  
552 spectrometer equipped with a TCI cryogenic probe. Spectra were processed with the software  
553 NMRPipe and visualized using Sparky NMR. The concentrations of <sup>2</sup>H, <sup>15</sup>N, <sup>13</sup>C-labeled

554 proSP-C was 288  $\mu\text{mol L}^{-1}$  in 20  $\text{mmol L}^{-1}$  ammonium acetate pH 7.2 and 229  $\mu\text{mol L}^{-1}$  in 20  
555  $\text{mmol L}^{-1}$  ammonium acetate pH 5.5, both in 90%  $\text{H}_2\text{O}/10\% \text{D}_2\text{O}$ .

556

### 557 **Circular dichroism and fluorescence spectroscopy and aggregation analyses**

558 CD spectra were recorded in 1 mm path length quartz cuvettes at 25°C from 260 to 185 nm in  
559 a J-1500 Circular Dichroism Spectrophotometer (JASCO, Japan) with a protein concentration  
560 of 4.2–10  $\mu\text{mol L}^{-1}$ . The bandwidth was set to 1 nm, data pitch 0.5 nm, and scanning speed  
561 50 nm  $\text{min}^{-1}$ . The spectra shown are averages of five consecutive scans.

562

563 Citrate synthase from porcine heart (Sigma-Aldrich, Germany) was diluted in 40  $\text{mmol L}^{-1}$   
564 HEPES/KOH pH 7.5 to 600  $\text{nmol L}^{-1}$  (calculated from a molecular weight of 85 kDa  
565 corresponding to a dimer(69)) and then equilibrated at 45°C with and without different  
566 concentrations of rh Bri2 BRICHOS D148N oligomer or proSP-C BRICHOS variants. The  
567 aggregation kinetics were measured by reading the apparent increase in absorbance at 360 nm  
568 under quiescent conditions using a microplate reader (FLUOStar Galaxy from BMG Labtech,  
569 Offenberg, Germany).

570

571 One  $\mu\text{mol L}^{-1}$ , calculated for the monomeric subunit, of different rh BRICHOS in 20  $\text{mmol L}^{-1}$   
572 NaPi pH 8.0 or pH 6.0 were incubated at 25°C with 2  $\mu\text{mol L}^{-1}$  bis-ANS (4,4'-  
573 Bis(phenylamino)-[1,1'-binaphthalene]-5,5'-disulfonic acid dipotassium salt) for 10 min, and  
574 the fluorescence emission spectra were recorded from 420 to 600 nm after excitation at 395  
575 nm with the Infinite M1000 plate reader (Tecan, Austria). Rh Bri2 BRICHOS T206W  
576 monomers were diluted to 2  $\mu\text{mol L}^{-1}$  by using 20  $\text{mmol L}^{-1}$  NaPi containing 0.2  $\text{mmol L}^{-1}$   
577 EDTA with different pH in the final samples in the range of 6.3–8.0. For tryptophan  
578 fluorescence measurements, samples were prepared in duplicates with a volume of 150  $\mu\text{L}$ .  
579 Samples were excited at 280 nm (5  $\mu\text{m}$  bandwidth) and fluorescence emission from 300–400  
580 nm (10  $\mu\text{m}$  bandwidth, 1 nm step interval) was recorded on black polystyrene flat-bottom 96-  
581 well plates (Costar) using a spectrofluorometer (Tecan Saphire 2). For the final fluorescence  
582 intensities, the results were corrected by subtracting the background fluorescence of the  
583 buffer.

584

### 585 **Transmission electron microscopy imaging of rh Bri2 BRICHOS D148N oligomers and** 586 **single particle processing**

587 Rh Bri2 BRICHOS D148N oligomers after SEC isolation were immediately stored on ice  
588 followed by grid preparation. Aliquots (4  $\mu$ L) were adsorbed onto glow-discharged  
589 continuous carbon-coated copper grids (400 mesh, Analytical Standards) for one min. The  
590 grids were subsequently blotted with filter paper, washed with two drops of milli-Q water,  
591 and negatively stained with one drop of 2% (w/v) uranyl acetate for 45 s before final blotting  
592 and air-drying. The sample was imaged using a Jeol JEM2100F field emission gun  
593 transmission electron microscope (Jeol, Japan) operating at 200 kV. Single micrographs for  
594 evaluating the quality of the sample were recorded on a Tietz 4k  $\times$  4k CCD camera, TVIPS  
595 (Tietz Video and Image Processing Systems, GmbH, Gauting, Germany) at magnification  
596 of  $\times$  85 200 (1.76 $\text{\AA}$  per pixel) and 1.0–2.8  $\mu$ m defocus. A total of 16 micrographs were  
597 recorded for single particle analysis. All 16 micrographs were imported to EMAN2 (version  
598 2.3) for further processing(70). After importing and estimating defocus with e2evalimage.py,  
599 single particles in different orientations were selected from the images using e2boxer.py in  
600 manual mode (11 094 particles, after one more manual selection, 10 223 particles were left).  
601 For each image, the contrast transfer function (CTF) parameters were estimated on boxed out  
602 regions (containing particles, 168 $\times$ 168) using e2ctf.auto.py program. A reference-free 2D  
603 classification based on the selected 10 223 phase-flipped particles (low-pass filtered to 20  $\text{\AA}$ )  
604 was performed using e2refine2d.py. The 2D classes show an approximate 2-fold symmetry,  
605 which is consistent with both the results of rh wildtype Bri2 BRICHOS oligomer and the  
606 biochemical data. Generated 2D classes were used as the input for building the 3D initial  
607 model using e2initialmodel.py. 3D refinement was performed in several rounds using  
608 e2refine\_easy.py applying D2 symmetry aiming at a final resolution of 15  $\text{\AA}$ . The first two  
609 rounds of 3D refinements were performed with pixel size of 3.52  $\text{\AA}$  after binning the data by  
610 a linear factor 2. In the last round of refinement, the data was resampled to 2.464  $\text{\AA}$  per pixel.  
611 The final map from the first round of refinements was used as model in the second, and the  
612 final map from the second round of refinements was used as model in the third. The  
613 resolution was determined based on a Fourier shell correlation (FSC) value of 0.143(71),  
614 following the gold standard FSC procedure implemented in EMAN2(72).  
615

## 616 **BRICHOS and A $\beta$ 42 monomer interaction monitored by surface plasmon resonance**

617 A $\beta$ 42 monomers were immobilized by amine coupling onto flowcell 4 on a CM5 sensor chip  
618 (GE Healthcare) using a BIACore 3000 instrument (BIACore AB). A reference surface was  
619 prepared on flowcell 3 using the same coupling protocol but without protein injected. The

immobilization was performed at a flow rate of 20  $\mu\text{L min}^{-1}$  with 20 mmol  $\text{L}^{-1}$  sodium phosphate pH 8.0 containing 0.2 mmol  $\text{L}^{-1}$  EDTA as running buffer, and the other details were set according to the manufacturer's instructions. After immobilization with a final response level of 727 RU, the flow-cells were stabilized over night in running buffer (10 mmol  $\text{L}^{-1}$  HEPES pH 7.5 containing 150 mmol  $\text{L}^{-1}$  NaCl and 0.2 mmol  $\text{L}^{-1}$  EDTA) at a flow rate of 20  $\mu\text{L min}^{-1}$ . For binding analysis, 25  $\mu\text{mol L}^{-1}$  rh wildtype proSP-C BRICHOS or the D105N mutant in 10 mmol  $\text{L}^{-1}$  HEPES pH 7.5 containing 150 mmol  $\text{L}^{-1}$  NaCl and 0.2 mmol  $\text{L}^{-1}$  EDTA were injected in over the chip surfaces at 25°C at a flow rate of 20  $\mu\text{L min}^{-1}$  for 3 min, respectively. 10 mmol  $\text{L}^{-1}$  NaOH was used for further chip surface regeneration. For kinetic analysis, different concentrations of rh proSP-C BRICHOS D105N mutant in running buffer, *i.e.* 0, 1.56, 3.13, 6.25, 12.5, 25, 50 and 100  $\mu\text{mol L}^{-1}$ , were individually injected in over the chip surfaces at 25°C at a flow rate of 20  $\mu\text{L min}^{-1}$ . 30 mmol  $\text{L}^{-1}$  NaOH was used for further chip surface regeneration. In all experiments, the response from the blank surface was subtracted from the immobilized surface response, the baselines of the sensorgrams were adjusted to zero and buffer spikes were excluded.

635

Steady state apparent affinities for rh proSP-C BRICHOS D105N mutant to immobilised A $\beta$ 42 monomers were estimated by plotting the maximum binding response versus BRICHOS concentrations. The baseline of the sensorgrams were adjusted to zero and buffer spikes were excluded for global fits to reflect the binding affinity. Since the response signals of the two lowest protein concentrations (*i.e.*, 1.56 and 3.13  $\mu\text{mol L}^{-1}$ ) used in kinetic analysis were too weak, only sensorgrams obtained from rh proSP-C BRICHOS D105N mutant ranging from 6.25  $\mu\text{mol L}^{-1}$  to 100  $\mu\text{mol L}^{-1}$  were included in the global fits. The dissociation was globally fitted to a biexponential model as described by Eq. (1)(28, 73):

$$644 \quad R(t) = R_1(xe^{-k_{d1}(t-t_1)} + (1-x)e^{-k_{d2}(t-t_1)}) \quad \text{Eq. (1)}$$

where  $R_1$  is the response signal at the starting time for the dissociation phase  $t_1$ , and  $x$  is between 0 and 1.  $k_{d1}$  and  $k_{d2}$  are the dissociation rate constants for the fast and slow dissociation phases, respectively. The global fitted value  $k_{d2}$  was used to calculate the apparent  $K_D$  value.

The association phase was fitted to Eq. (2)(28):

$$650 \quad R(t) = R_f + (R_0 - R_f)e^{-k_{obs}t} \quad \text{Eq. (2)}$$

651 where  $R_0$  and  $R_f$  are the initial and final response signal of the association phase, respectively.

652  $k_{obs}$  is the observed rate constant described by Eq. (3)(28, 73):

653  $k_{obs} = ck_a + k_d$  Eq. (3)

654 where  $c$  is the protein concentration,  $k_a$  is the association rate constant, and  $k_d$  from this  
655 analysis is related to secondary binding artifacts corresponding to  $k_{d1}$ . Linear regression was  
656 used to determine  $k_a$ . The apparent  $K_D$  value was calculated as ratio of the dissociation rate  
657 constant and association rate constant.

658

### 659 **A $\beta$ 42 monomer preparation and ThT assay**

660 Recombinant Met-A $\beta$ (1–42), here referred to as A $\beta$ 42, was produced in BL21\*(DE3) pLysS  
661 *E. coli* (B strain) cells and purified by ion exchange(32). The purified A $\beta$ 42 peptides were  
662 lyophilized and re-dissolved in 20 mmol L<sup>-1</sup> Tris pH 8.0 with 7 mol L<sup>-1</sup> Gdn-HCl, and the  
663 monomers were isolated in 20 mmol L<sup>-1</sup> sodium phosphate pH 8.0 with 0.2 mmol L<sup>-1</sup> EDTA  
664 by a Superdex 30 column 26/600 (GE Healthcare, UK). The concentration of monomeric  
665 A $\beta$ 42 was calculated with using an extinction coefficient of 1 424 M<sup>-1</sup> cm<sup>-1</sup> for (A<sub>280</sub>–A<sub>300</sub>).  
666 For A $\beta$ 42 fibrillization kinetics analysis, 20  $\mu$ L solution containing 10  $\mu$ mol L<sup>-1</sup> ThT, 3  $\mu$ mol  
667 L<sup>-1</sup> A $\beta$ 42 monomer and different concentrations of rh BRICHOS at molar ratios 0, 10, 30, 50,  
668 70 or 100 % (relative to A $\beta$ 42 monomer molar concentration), were added to each well of  
669 half-area 384-well microplates with clear bottom (Corning Glass 3766, USA), and incubated  
670 at 37°C under quiescent conditions. The ThT fluorescence was recorded using a 440 nm  
671 excitation filter and a 480 nm emission filter using a microplate reader (FLUOStar Galaxy  
672 from BMG Labtech, Offenberg, Germany). For A $\beta$ 42 seeds preparation, 3  $\mu$ mol L<sup>-1</sup> A $\beta$ 42  
673 monomers were incubated for about 20 h at 37°C, and the fibrils were then sonicated in a  
674 water bath for 3 min. For seeding of A $\beta$ 42 fibrillization, 20  $\mu$ L solution containing 10  $\mu$ mol  
675 L<sup>-1</sup> ThT, 3  $\mu$ mol L<sup>-1</sup> A $\beta$ 42, different concentrations of rh BRICHOS at 0, 10, 50, 70 and  
676 100 %, and 0.6  $\mu$ mol L<sup>-1</sup> seeds (calculated from the original A $\beta$ 42 monomer concentration)  
677 were added at 4°C to each well in triplicate of 384-well microplates with clear bottom  
678 (Corning Glass 3766, USA) and immediately incubated at 37°C under quiescent conditions.  
679 The elongation rate constant  $k_+$  in the presence of rh BRICHOS was calculated from the  
680 highly seeded experiments. The initial slope of the concave aggregation traces was  
681 determined by a linear fit of the first ~20 min traces. For all the experiments, aggregation  
682 traces were normalized and averaged using four or three replicates, and data defining one

683 dataset was recorded from the same plate at the same time, and all the ThT data was from the  
684 same batch of A $\beta$ 42 peptide.

685

## 686 Analysis of A $\beta$ 42 aggregation kinetics

687 Fibrillization traces of A $\beta$ 42 with and without different concentrations of rh BRICHOS were  
688 fitted to a sigmoidal equation Eq. (4)(32, 33), where the half time  $\tau_{1/2}$  and the maximal  
689 growth rate  $r_{max}$  were extracted:

690 
$$F = F_0 + A/(1 + \exp[r_{max}(\tau_{1/2} - t)]) \quad \text{Eq. (4)}$$

691 where  $A$  the amplitude and  $F_0$  the base value.

692

693 To dissect the molecular mechanism underlying BRICHOS counteracting A $\beta$ 42 aggregation,  
694 the fibrillization traces were globally fitted by Eq. (5)(27):

$$\frac{M(t)}{M(\infty)} = 1 - \left( \frac{B_+ + C_+}{B_+ + C_+ \cdot \exp(\kappa t)} \cdot \frac{B_- + C_+ \cdot \exp(\kappa t)}{B_- + C_+} \right)^{\frac{k_\infty^2}{\kappa \tilde{k}_\infty}} \cdot \exp(-\kappa t) \quad \text{Eq. (5)}$$

695 where  $M(t)$  is the total fibril mass concentration, and the intermediate coefficients are  
696 functions of  $\lambda$  and  $\kappa$ , and  $n_c$  and  $n_2$  are the reaction orders for primary and secondary  
697 nucleation, respectively:

$$\begin{aligned} C_\pm &= \pm \lambda^2 / 2\kappa^2 \\ k_\infty &= \sqrt{2\kappa^2/(n_2(n_2 + 1)) + 2\lambda^2/n_c} \\ \tilde{k}_\infty &= \sqrt{k_\infty^2 - 4C_+C_-\kappa^2} \\ B_\pm &= (k_\infty \pm \tilde{k}_\infty)/2\kappa \\ \lambda &= \sqrt{2 \cdot k_+ k_n \cdot m(0)^{n_c}} \\ \kappa &= \sqrt{2 \cdot k_+ k_2 \cdot m(0)^{n_2+1}} \end{aligned}$$

698 The microscopic rate constants  $k_n$ ,  $k_+$ , and  $k_2$  are for primary nucleation, elongation, and  
699 secondary nucleation, respectively. The kinetic data were globally fitted to Eq. (5), where the  
700 fits were partially constrained with one fitting parameter held to a constant value, resulting in  
701 that only one rate constant ( $k_n$ ,  $k_+$  or  $k_2$ ) is the sole fitting parameter(32, 33). To investigate  
702 the generation of nucleation units, according to the nucleation rate  $r_n(t)$ (27):

703 
$$r_n(t) = k_n m(t)^{n_c} + k_2 M(t) m(t)^{n_2},$$

704 the total number of nucleation units was calculated by integrating the nucleation rate  $r_n(t)$   
705 over the reaction.

706

## 707 **Immunogold staining of A $\beta$ 42 fibrils and transmission electron microscopy analysis**

708 Five  $\mu\text{mol L}^{-1}$  A $\beta$ 42 monomer was incubated at 37°C with 100% rh wildtype proSP-C  
709 BRICHOS and the D105N mutant overnight, and the fibrils were collected at 4°C by  
710 centrifugation for 1 h at 22 000 $\times g$ . The fibrils were gently resuspended in 20  $\mu\text{L}$  1 $\times$ TBS, of  
711 which 2  $\mu\text{L}$  were applied to carbon coated copper grids, and incubated for about 5 min.  
712 Excess solution was removed and the grids were blocked by incubation in 1% BSA in 1 $\times$ TBS  
713 for 30 min, followed by 3 $\times$ 10 min washing by 1 $\times$ TBS. The grids were then incubated with  
714 polyclonal antibody against human proSP-C (SFTPC) (1:200 dilution, Atlas Antibodies)  
715 overnight at 4°C, and washed 3 $\times$ 10 min with 1 $\times$ TBS. Finally, the grids were incubated with  
716 anti-rabbit IgG-gold coupled to 20 nm gold particles (1:40 dilution, BBI Solutions) for 2 h at  
717 room temperature, and washed 5 $\times$ 10 min with 1 $\times$ TBS. Excess solution was removed, and 2  
718  $\mu\text{L}$  of 2.5% uranyl acetate was added to each grid (kept about 20 s). Excess solution was  
719 removed, and the grids were air-dried at room temperature, and analysed by transmission  
720 electron microscopy (TEM, Jeol JEM2100F at 200 kV).

721

## 722 **Electrophysiological recordings**

723 All the animal experiments were carried out in accordance with the ethical permit granted by  
724 Norra Stockholm's Djurförsökssetiska Nämnd (dnr N45/13). C57BL/6 mice of either sex  
725 (postnatal days 14–23, supplied from Charles River, Germany) were used in the experiments.  
726 Before sacrificed, all the mice were anaesthetized deeply using isoflurane.

727

728 The brain was dissected out and placed in modified ice-cold ACSF (artificial cerebrospinal  
729 fluid). The ACSF contained 80  $\text{mmol L}^{-1}$  NaCl, 24  $\text{mmol L}^{-1}$  NaHCO<sub>3</sub>, 25  $\text{mmol L}^{-1}$  glucose,  
730 1.25  $\text{mmol L}^{-1}$  NaH<sub>2</sub>PO<sub>4</sub>, 1  $\text{mmol L}^{-1}$  ascorbic acid, 3  $\text{mmol L}^{-1}$  NaPyruvate, 2.5  $\text{mmol L}^{-1}$   
731 KCl, 4  $\text{mmol L}^{-1}$  MgCl<sub>2</sub>, 0.5  $\text{mmol L}^{-1}$  CaCl<sub>2</sub> and 75  $\text{mmol L}^{-1}$  sucrose. Horizontal sections  
732 (350  $\mu\text{m}$  thick) of the ventral hippocampi from both hemispheres were sliced with a Leica  
733 VT1200S vibratome (Microsystems, Sweden). The sections were immediately transferred to  
734 a submerged incubation chamber containing standard ACSF: 124  $\text{mmol L}^{-1}$  NaCl, 30  $\text{mmol L}^{-1}$   
735 NaHCO<sub>3</sub>, 10  $\text{mmol L}^{-1}$  glucose, 1.25  $\text{mmol L}^{-1}$  NaH<sub>2</sub>PO<sub>4</sub>, 3.5  $\text{mmol L}^{-1}$  KCl, 1.5  $\text{mmol L}^{-1}$   
736 MgCl<sub>2</sub> and 1.5  $\text{mmol L}^{-1}$  CaCl<sub>2</sub>. The chamber was held at 34°C for at least 20 min after

737 dissection and it was subsequently cooled to room temperature (~22°C) for a minimum of 40  
738 min. Proteins (A $\beta$ 42 and rh BRICHOS) were first added to the incubation solution for 15 min,  
739 and then the slices were transferred to the interface-style recording chamber for extracellular  
740 recordings. During the incubation, slices were supplied continuously with carbogen gas (5%  
741 CO<sub>2</sub>, 95% O<sub>2</sub>) bubbled into the ACSF.

742

743 Recordings were performed with borosilicate glass microelectrodes in hippocampal area CA3,  
744 pulled to a resistance of 3–5 M $\Omega$ , filled with ACSF and placed in stratum pyramidale. Local  
745 field potentials (LFP,  $\gamma$  oscillations) were recorded at 32°C in an interface-type chamber  
746 (perfusion rate 4.5 mL per minute) and elicited by applying kainic acid (100 nmol L<sup>-1</sup>, Tocris).  
747 The oscillations were stabilized for 20 min before any recordings. No A $\beta$ 42, rh Bri2  
748 BRICHOS R221E species or combinations thereof were present in the recording chamber  
749 either during  $\gamma$  oscillations stabilization, or during electrophysiological recordings. The  
750 interface chamber recording solution contained 124 mmol L<sup>-1</sup> NaCl, 30 mmol L<sup>-1</sup> NaHCO<sub>3</sub>,  
751 10 mmol L<sup>-1</sup> glucose, 1.25 mmol L<sup>-1</sup> NaH<sub>2</sub>PO<sub>4</sub>, 3.5 mmol L<sup>-1</sup> KCl, 1.5 mmol L<sup>-1</sup> MgCl<sub>2</sub> and  
752 1.5 mmol L<sup>-1</sup> CaCl<sub>2</sub>.

753

754 Interface chamber LFP recordings were carried out by a 4-channel amplifier/signal  
755 conditioner M102 amplifier (Electronics lab, University of Cologne, Germany). The signals  
756 were sampled at 10 kHz, conditioned using a Hum Bug 50 Hz noise eliminator (LFP signals  
757 only; Quest Scientific, North Vancouver, BC, Canada), software low-pass filtered at 1 kHz,  
758 digitized and stored using a Digidata 1322A and Clampex 9.6 software (Molecular Devices,  
759 CA, USA).

760

761 Power spectral density plots (from 60 s long LFP recordings) were calculated using  
762 Axograph X (Kagi, Berkeley, CA, USA) in averaged Fourier-segments of 8 192 points.  
763 Oscillation power was calculated from the integration of the power spectral density from 20  
764 to 80 Hz.

765

## 766 **Statistics and reproducibility**

767 The electrophysiological data is presented as means  $\pm$  standard errors of the means. Prior  
768 statistical analysis all the data was subjected to outlier determination and removal with the  
769 ROUT method (Q = 1%) followed by D'Agostino & Pearson omnibus normality test. Based

770 on the previous experience with the outliers and overall sample behaviour, sample size was  
771 determined based on previous studies performed in an interface-type chamber(27, 32, 33, 47,  
772 74, 75). Each experimental round was performed with parallel controls (Control KA and  
773 A $\beta$ 42) from the same animal and randomized preparations (slices incubated with A $\beta$ 42 + rh  
774 proSP-C BRICHOS D105N, + wildtype rh proSP-C BRICHOS, + rh Bri2-BRICHOS D148N  
775 monomers or + wildtype rh Bri2-BRICHOS). For comparison purposes data from Control  
776 KA and A $\beta$ 42 was pooled from interleaved slices recorded in these conditions. The number  
777 of recorded slices per condition (at least from 3–5 mice) are shown in the corresponding  
778 figure legend and source data file. Kruskal-Wallis test followed by Dunn's multiple  
779 comparisons were carried out due to the non-parametric nature- or relatively small size of  
780 some data. Comparison of the preventative efficacies of rh Bri2-BRICHOS D148N  
781 monomers and rh proSP-C BRICHOS D105N was assessed with the Mann Whitney test.  
782 Significance levels are \*  $p<0.05$ , \*\*  $p<0.01$ , and \*\*\* $p<0.001$ . The ThT assay data are  
783 presented as means  $\pm$  standard deviation, and the aggregation traces are averaged from four  
784 or three replicates.

785 **References**

- 786 1. Sipe JD, Benson MD, Buxbaum JN, Ikeda SI, Merlini G, Saraiva MJ, et al. Amyloid fibril  
787 proteins and amyloidosis: chemical identification and clinical classification International  
788 Society of Amyloidosis 2016 Nomenclature Guidelines. *Amyloid*. 2016;23(4):209-13.
- 789 2. Landreh M, Sawaya MR, Hipp MS, Eisenberg DS, Wuthrich K, Hartl FU. The formation,  
790 function and regulation of amyloids: insights from structural biology. *J Intern Med*.  
791 2016;280(2):164-76.
- 792 3. Bucciantini M, Giannoni E, Chiti F, Baroni F, Formigli L, Zurdo J, et al. Inherent toxicity  
793 of aggregates implies a common mechanism for protein misfolding diseases. *Nature*.  
794 2002;416(6880):507-11.
- 795 4. Goldschmidt L, Teng PK, Riek R, Eisenberg D. Identifying the amyloome, proteins  
796 capable of forming amyloid-like fibrils. *Proc Natl Acad Sci U S A*. 2010;107(8):3487-92.
- 797 5. Balchin D, Hayer-Hartl M, Hartl FU. In vivo aspects of protein folding and quality  
798 control. *Science*. 2016;353(6294):aac4354.
- 799 6. Soti C, Csermely P. Aging and molecular chaperones. *Exp Gerontol*.  
800 2003;38(10):1037-40.
- 801 7. Wolff S, Weissman JS, Dillin A. Differential scales of protein quality control. *Cell*.  
802 2014;157(1):52-64.
- 803 8. Hipp MS, Kasturi P, Hartl FU. The proteostasis network and its decline in ageing. *Nat  
804 Rev Mol Cell Biol*. 2019.
- 805 9. Sarparanta J, Jonson PH, Kawan S, Udd B. Neuromuscular Diseases Due to Chaperone  
806 Mutations: A Review and Some New Results. *Int J Mol Sci*. 2020;21(4).

807 10. Almeida-Souza L, Goethals S, de Winter V, Dierick I, Gallardo R, Van Durme J, et al.  
808 Increased monomerization of mutant HSPB1 leads to protein hyperactivity in Charcot-  
809 Marie-Tooth neuropathy. *J Biol Chem.* 2010;285(17):12778-86.  
810 11. Zhang YW, Thompson R, Zhang H, Xu H. APP processing in Alzheimer's disease. *Mol*  
811 *Brain.* 2011;4:3.  
812 12. Westermark P, Andersson A, Westermark GT. Islet amyloid polypeptide, islet  
813 amyloid, and diabetes mellitus. *Physiol Rev.* 2011;91(3):795-826.  
814 13. Häggqvist B, Näslund J, Sletten K, Westermark GT, Mucchiano G, Tjernberg LO, et al.  
815 Medin: an integral fragment of aortic smooth muscle cell-produced lactadherin forms the  
816 most common human amyloid. *Proc Natl Acad Sci U S A.* 1999;96(15):8669-74.  
817 14. Hedlund J, Johansson J, Persson B. BRICHOS - a superfamily of multidomain proteins  
818 with diverse functions. *BMC Res Notes.* 2009;2:180.  
819 15. Sanchez-Pulido L, Devos D, Valencia A. BRICHOS: a conserved domain in proteins  
820 associated with dementia, respiratory distress and cancer. *Trends Biochem Sci.*  
821 2002;27(7):329-32.  
822 16. Willander H, Askarieh G, Landreh M, Westermark P, Nordling K, Keranen H, et al.  
823 High-resolution structure of a BRICHOS domain and its implications for anti-amyloid  
824 chaperone activity on lung surfactant protein C. *Proc Natl Acad Sci U S A.* 2012;109(7):2325-  
825 9.  
826 17. Knight SD, Presto J, Linse S, Johansson J. The BRICHOS domain, amyloid fibril  
827 formation, and their relationship. *Biochemistry.* 2013;52(43):7523-31.  
828 18. Buxbaum JN, Johansson J. Transthyretin and BRICHOS: The Paradox of  
829 Amyloidogenic Proteins with Anti-Amyloidogenic Activity for Abeta in the Central Nervous  
830 System. *Front Neurosci.* 2017;11:119.  
831 19. Martin L, Fluhrer R, Reiss K, Kremmer E, Saftig P, Haass C. Regulated intramembrane  
832 proteolysis of Bri2 (Itm2b) by ADAM10 and SPPL2a/SPPL2b. *J Biol Chem.* 2008;283(3):1644-  
833 52.  
834 20. Del Campo M, Hoozemans JJ, Dekkers LL, Rozemuller AJ, Korth C, Muller-Schiffmann  
835 A, et al. BRI2-BRICHOS is increased in human amyloid plaques in early stages of Alzheimer's  
836 disease. *Neurobiol Aging.* 2014;35(7):1596-604.  
837 21. Oskarsson ME, Hermansson E, Wang Y, Welsh N, Presto J, Johansson J, et al.  
838 BRICHOS domain of Bri2 inhibits islet amyloid polypeptide (IAPP) fibril formation and toxicity  
839 in human beta cells. *Proc Natl Acad Sci U S A.* 2018;115(12):E2752-E61.  
840 22. Vidal R, Revesz T, Rostagno A, Kim E, Holton JL, Bek T, et al. A decamer duplication in  
841 the 3' region of the BRI gene originates an amyloid peptide that is associated with dementia  
842 in a Danish kindred. *Proc Natl Acad Sci U S A.* 2000;97(9):4920-5.  
843 23. Vidal R, Frangione B, Rostagno A, Mead S, Revesz T, Plant G, et al. A stop-codon  
844 mutation in the BRI gene associated with familial British dementia. *Nature.*  
845 1999;399(6738):776-81.  
846 24. Willander H, Presto J, Askarieh G, Biverstal H, Frohm B, Knight SD, et al. BRICHOS  
847 domains efficiently delay fibrillation of amyloid beta-peptide. *J Biol Chem.*  
848 2012;287(37):31608-17.  
849 25. Nerelius C, Gustafsson M, Nordling K, Larsson A, Johansson J. Anti-amyloid activity of  
850 the C-terminal domain of proSP-C against amyloid beta-peptide and medin. *Biochemistry.*  
851 2009;48(17):3778-86.



897 42. Yamamoto J, Suh J, Takeuchi D, Tonegawa S. Successful execution of working  
898 memory linked to synchronized high-frequency gamma oscillations. *Cell*. 2014;157(4):845-  
899 57.

900 43. Ribary U, Ioannides AA, Singh KD, Hasson R, Bolton JP, Lado F, et al. Magnetic field  
901 tomography of coherent thalamocortical 40-Hz oscillations in humans. *Proc Natl Acad Sci U  
902 S A*. 1991;88(24):11037-41.

903 44. Iaccarino HF, Singer AC, Martorell AJ, Rudenko A, Gao F, Gillingham TZ, et al. Gamma  
904 frequency entrainment attenuates amyloid load and modifies microglia. *Nature*.  
905 2016;540(7632):230-5.

906 45. Martorell AJ, Paulson AL, Suk HJ, Abdurrob F, Drummond GT, Guan W, et al. Multi-  
907 sensory Gamma Stimulation Ameliorates Alzheimer's-Associated Pathology and Improves  
908 Cognition. *Cell*. 2019;177(2):256-71.e22.

909 46. Kurudenkandy FR, Zilberter M, Biverstal H, Presto J, Honcharenko D, Stromberg R, et  
910 al. Amyloid-beta-induced action potential desynchronization and degradation of  
911 hippocampal gamma oscillations is prevented by interference with peptide conformation  
912 change and aggregation. *J Neurosci*. 2014;34(34):11416-25.

913 47. Andrade-Talavera Y, Chen G, Kurudenkandy FR, Johansson J, Fisahn A. Bri2 BRICHOS  
914 chaperone rescues impaired fast-spiking interneuron behavior and neuronal network  
915 dynamics in an AD mouse model in vitro. *Neurobiol Dis*. 2021;105514.

916 48. Khurana R, Coleman C, Ionescu-Zanetti C, Carter SA, Krishna V, Grover RK, et al.  
917 Mechanism of thioflavin T binding to amyloid fibrils. *J Struct Biol*. 2005;151(3):229-38.

918 49. Cohen SI, Vendruscolo M, Dobson CM, Knowles TP. From macroscopic  
919 measurements to microscopic mechanisms of protein aggregation. *J Mol Biol*. 2012;421(2-  
920 3):160-71.

921 50. Arosio P, Vendruscolo M, Dobson CM, Knowles TP. Chemical kinetics for drug  
922 discovery to combat protein aggregation diseases. *Trends Pharmacol Sci*. 2014;35(3):127-35.

923 51. Hawe A, Sutter M, Jiskoot W. Extrinsic fluorescent dyes as tools for protein  
924 characterization. *Pharm Res*. 2008;25(7):1487-99.

925 52. Casals C, Johansson H, Saenz A, Gustafsson M, Alfonso C, Nordling K, et al. C-terminal,  
926 endoplasmic reticulum-luminal domain of prosurfactant protein C - structural features and  
927 membrane interactions. *FEBS J*. 2008;275(3):536-47.

928 53. Prasad H, Rao R. Amyloid clearance defect in ApoE4 astrocytes is reversed by  
929 epigenetic correction of endosomal pH. *Proc Natl Acad Sci U S A*. 2018;115(28):E6640-E9.

930 54. Su Y, Chang PT. Acidic pH promotes the formation of toxic fibrils from beta-amyloid  
931 peptide. *Brain Res*. 2001;893(1-2):287-91.

932 55. Poon S, Rybchyn MS, Easterbrook-Smith SB, Carver JA, Pankhurst GJ, Wilson MR.  
933 Mildly acidic pH activates the extracellular molecular chaperone clusterin. *J Biol Chem*.  
934 2002;277(42):39532-40.

935 56. Decker Y, Nemeth E, Schomburg R, Chemla A, Fulop L, Menger MD, et al. Decreased  
936 pH in the aging brain and Alzheimer's disease. *Neurobiol Aging*. 2021;101:40-9.

937 57. Hagihara H, Catts VS, Katayama Y, Shoji H, Takagi T, Huang FL, et al. Decreased Brain  
938 pH as a Shared Endophenotype of Psychiatric Disorders. *Neuropsychopharmacology*.  
939 2018;43(3):459-68.

940 58. Letunic I, Khedkar S, Bork P. SMART: recent updates, new developments and status  
941 in 2020. *Nucleic Acids Res*. 2021;49(D1):D458-d60.

942 59. Huang Y, Niu B, Gao Y, Fu L, Li W. CD-HIT Suite: a web server for clustering and  
943 comparing biological sequences. *Bioinformatics*. 2010;26(5):680-2.

944 60. Mistry J, Chuguransky S, Williams L, Qureshi M, Salazar GA, Sonnhammer ELL, et al.  
945 Pfam: The protein families database in 2021. *Nucleic Acids Res.* 2021;49(D1):D412-d9.  
946 61. Eddy SR. Accelerated Profile HMM Searches. *PLoS Comput Biol.*  
947 2011;7(10):e1002195.  
948 62. Poska H. In vitro and in vivo studies of molecular chaperone activity against fibrillar  
949 and non-fibrillar protein aggregation. Tallinn: Tallinn University; 2020.  
950 63. Katoh K, Rozewicki J, Yamada KD. MAFFT online service: multiple sequence  
951 alignment, interactive sequence choice and visualization. *Brief Bioinform.* 2019;20(4):1160-6.  
952 64. Crooks GE, Hon G, Chandonia JM, Brenner SE. WebLogo: a sequence logo generator.  
953 *Genome Res.* 2004;14(6):1188-90.  
954 65. Stamatakis A. RAxML-VI-HPC: maximum likelihood-based phylogenetic analyses with  
955 thousands of taxa and mixed models. *Bioinformatics.* 2006;22(21):2688-90.  
956 66. Letunic I, Bork P. Interactive Tree Of Life (iTOL) v4: recent updates and new  
957 developments. *Nucleic Acids Res.* 2019;47(W1):W256-w9.  
958 67. Kronqvist N, Sarr M, Lindqvist A, Nordling K, Otikovs M, Venturi L, et al. Efficient  
959 protein production inspired by how spiders make silk. *Nat Commun.* 2017;8:15504.  
960 68. Johansson H, Eriksson M, Nordling K, Presto J, Johansson J. The Brichos domain of  
961 prosurfactant protein C can hold and fold a transmembrane segment. *Protein Sci.*  
962 2009;18(6):1175-82.  
963 69. Srere PA. Citrate-condensing enzyme-oxalacetate binary complex. Studies on its  
964 physical and chemical properties. *J Biol Chem.* 1966;241(9):2157-65.  
965 70. Tang G, Peng L, Baldwin PR, Mann DS, Jiang W, Rees I, et al. EMAN2: an extensible  
966 image processing suite for electron microscopy. *J Struct Biol.* 2007;157(1):38-46.  
967 71. Rosenthal PB, Henderson R. Optimal determination of particle orientation, absolute  
968 hand, and contrast loss in single-particle electron cryomicroscopy. *J Mol Biol.*  
969 2003;333(4):721-45.  
970 72. Scheres SH, Chen S. Prevention of overfitting in cryo-EM structure determination.  
971 *Nat Methods.* 2012;9(9):853-4.  
972 73. Rahman MM, Zetterberg H, Lendel C, Härd T. Binding of human proteins to amyloid-  
973 β protofibrils. *ACS Chem Biol.* 2015;10(3):766-74.  
974 74. Balleza-Tapia H, Crux S, Andrade-Talavera Y, Dolz-Gaiton P, Papadia D, Chen G, et al.  
975 TrpV1 receptor activation rescues neuronal function and network gamma oscillations from  
976 Abeta-induced impairment in mouse hippocampus in vitro. *Elife.* 2018;7.  
977 75. Kurudenkandy FR, Zilberter M, Biverstål H, Presto J, Honcharenko D, Strömberg R, et  
978 al. Amyloid-β-induced action potential desynchronization and degradation of hippocampal  
979 gamma oscillations is prevented by interference with peptide conformation change and  
980 aggregation. *J Neurosci.* 2014;34(34):11416-25.

981

982 **Acknowledgements**

983 **Funding:**

984 Olle Engkvists Stiftelse 192-522  
985 Petrus and Augusta Hedlunds Stiftelse M-2018-0998  
986 Swedish Alzheimer Foundation AF-836251

987 Åhlén-stiftelsens mC9h18  
988 Karolinska Institutet Research Foundation Grant 2020-01819  
989 Stiftelsen för Gamla Tjänarinnor 2019-00779  
990 Loo and Hans Osterman Foundation 2019-01130  
991 Geriatric Diseases Foundation at Karolinska Institutet 2020-02290  
992 Magnus Bergvall Foundation 2019-03010  
993 Swedish Research Council 2020-02434  
994 Swedish Brain Foundation FO2018-0312  
995 Center for Innovative Medicine (CIMED)  
996 Swedish Society for Medical Research P17-0047  
997 FORMAS 2020-01013  
998 Åke Wiberg Foundation M20-0148  
999 JPco-fuND/EU PETABC 2020-02905/EC 643417  
1000 FLPP lzp-2018/1-0275  
1001 Stiftelsen Sigurd och Elsa Goljes Minne LA2020-0031  
1002  
1003 **Author contributions:**  
1004 G.C., Y.A.T., X.Z., H.P., H.B., A.L., and N.K. performed experiments. S.H. and G.C. carried  
1005 out bioinformatic analyses and visualization. G.C., Y.A.T., X.Z., H.B., H.P., A.A., N.K.,  
1006 A.R., H.H., P. K., A.F., and J.J. analysed the data. G.C. and J.J. conceived the study. G.C.  
1007 and J.J. wrote the paper. All authors discussed the results and commented on the manuscript.  
1008  
1009 **Competing interests:**  
1010 The authors declare no competing financial interests.  
1011  
1012 **Data and materials availability:**  
1013 The density map of the Bri2 BRICHOS D148N oligomer have been deposited in the Electron  
1014 Microscopy Data Bank (EMDB) under the accession code EMD-13005. All data and  
1015 materials related to this paper are available from G.C. (gefei.chen@ki.se).  
1016  
1017  
1018  
1019  
1020

1021

1022

1023

1024

1025

1026

1027

1028

1029

1030

1031

1032

1033

1034

1035

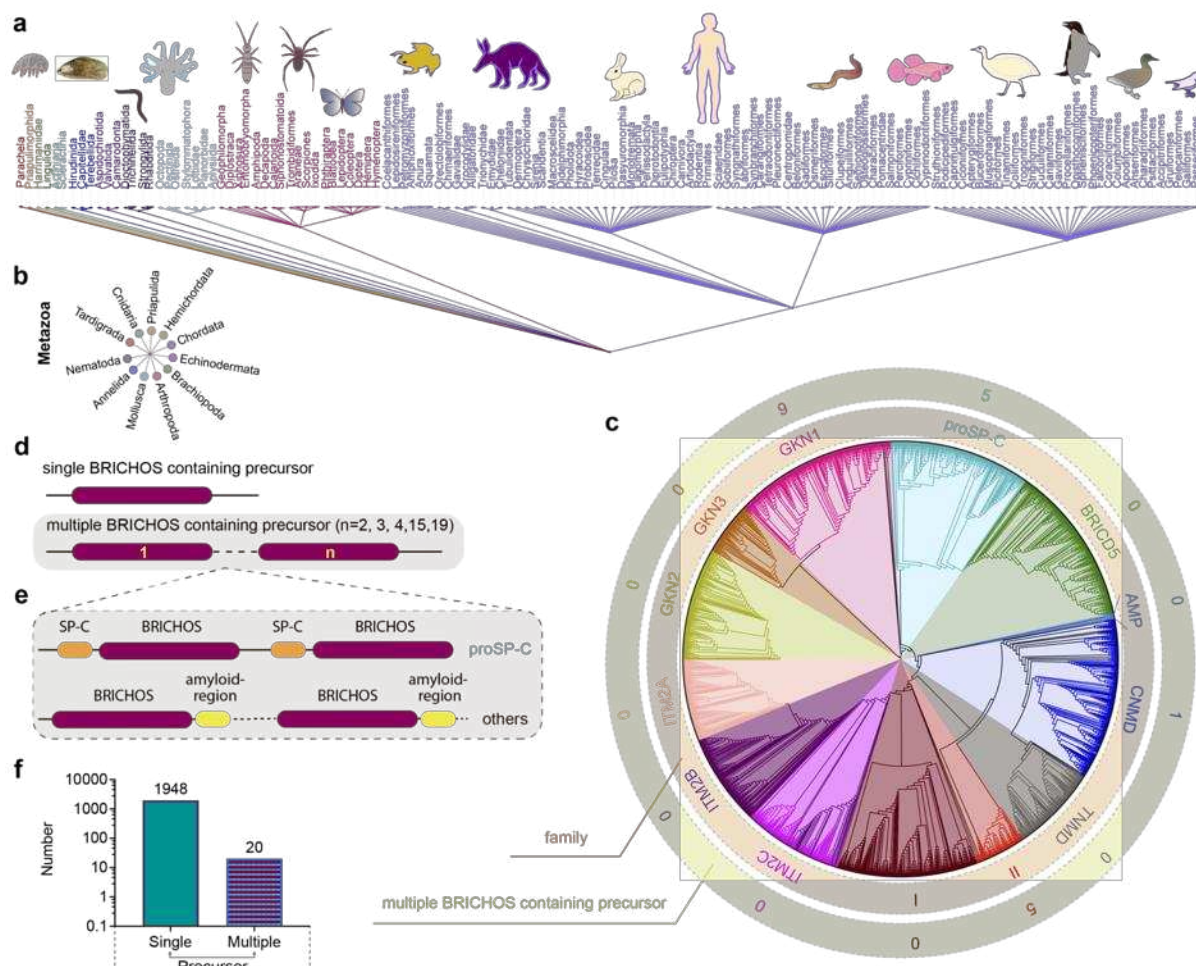
1036

1037

1038

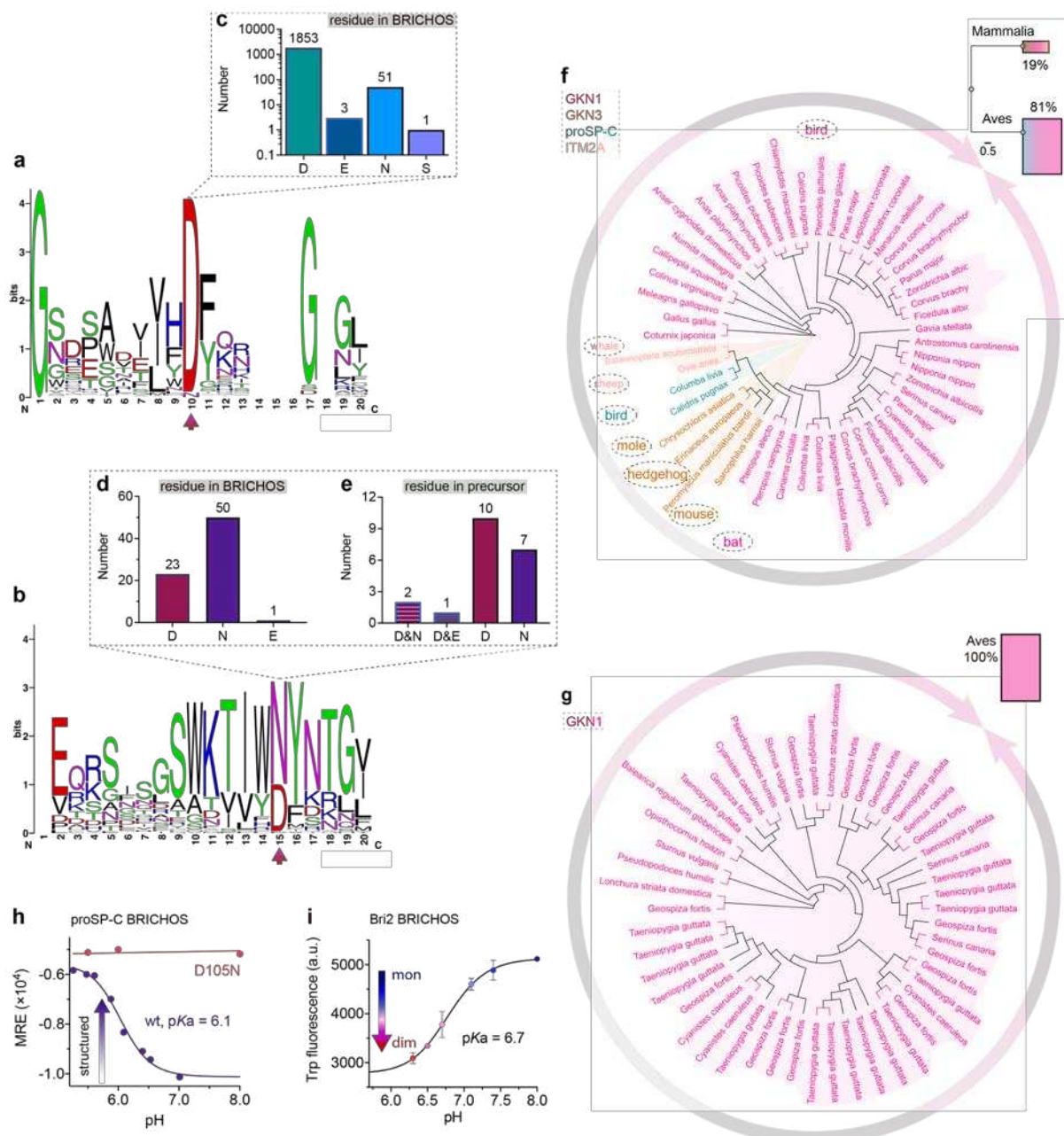
1039

1040 **Figures**



1041

**Fig. 1. Evolutionary analyses of the BRICHOS domain.** (a) The common taxonomy tree for all species containing BRICHOS domain precursors. The 3 355 BRICHOS precursors are distributed in a broad range of species, including worms, insects to human, and which belong to eleven metazoan phyla (b). (c) The selected 2 019 BRICHOS domains are grouped into thirteen families (inner ring), with bootstraps shown in **Supplementary Figure 1**. The outer ring shows the number of cases of occurrence of multiple BRICHOS domains in the respective families. (d) Architecture of proproteins containing single and up to nineteen multiple BRICHOS domains. The detailed architectures for each case are shown in **Supplementary Figure 2**. (e) the multiple BRICHOS domains showed there are a few BRICHOS containing proproteins that contain multiple BRICHOS domains along with representatives of their corresponding amyloid-prone regions. The true domain size is not proportional to the schematic bar. (f) The number of proproteins that contain single or multiple BRICHOS domains. 1 948 out of 1 968 proproteins contain a single BRICHOS domain while the others contain multiple BRICHOS domains.



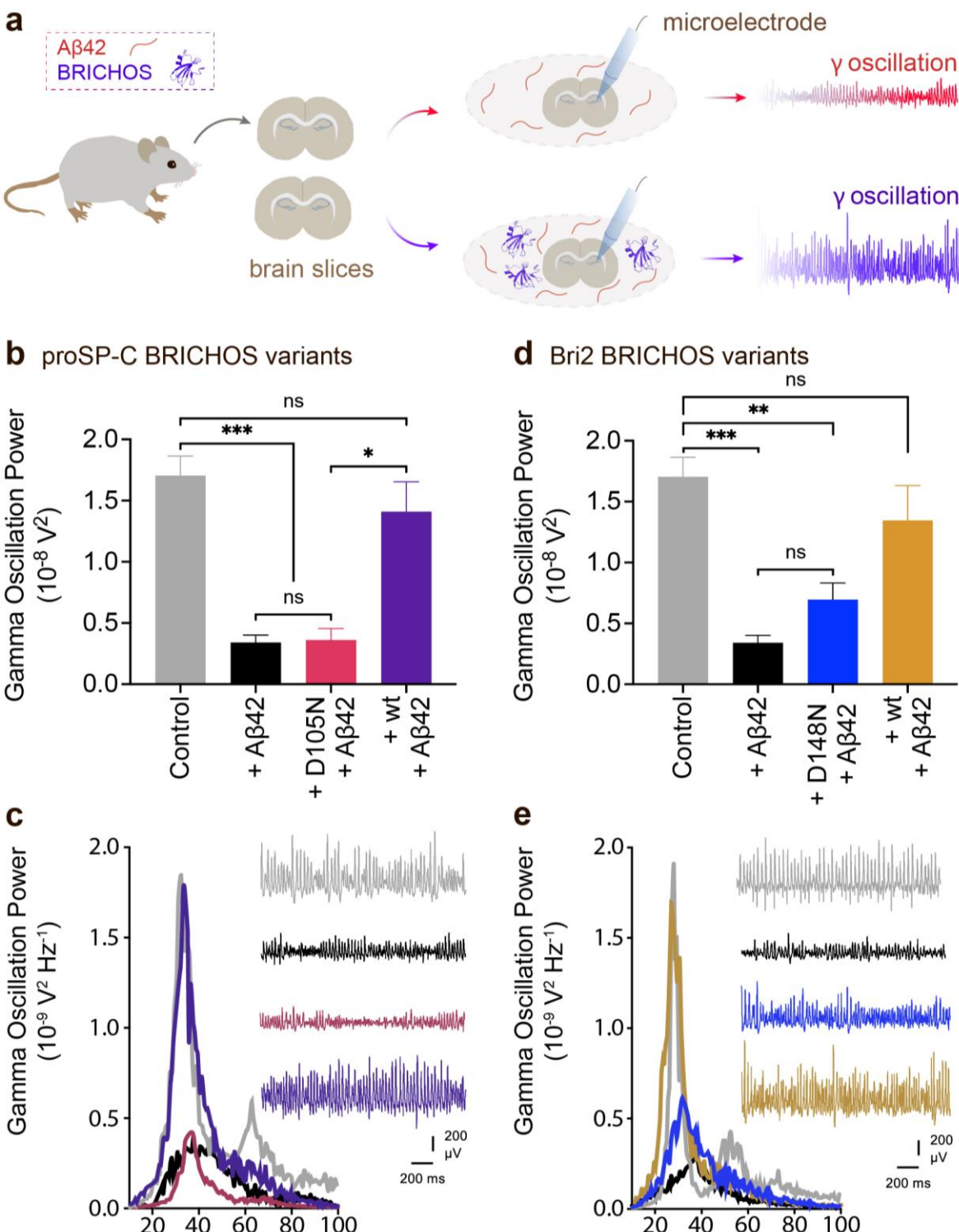
1056

1057 **Fig. 2. BRICHOS domain sequence analysis and species distribution.** (a) WebLogo  
1058 representation of amino acid sequence alignments of the 1908 single BRICHOS domains,  
1059 surrounding the conserved Asp (red arrow). The height of the amino acid stack represents the  
1060 sequence conservation, while the height of symbols within each stack indicates the relative  
1061 frequency of each residue and the total height of the letters is given in bits. (b) WebLogo  
1062 representation as in panel (a) of sequence alignments of the 74 multiple BRICHOS domains.  
1063 (c) The residue distribution at the position of the conserved Asp in single BRICHOS domains.  
1064 (d) The residue distribution at the position of the conserved Asp in multiple BRICHOS  
1065 domains. (e) The consistency of Asp or Asn, or the combination of Asp and Asn (or Glu) in  
1066 individual multiple BRICHOS containing precursor. (f) Family and species distributions of

1067 cases that contain Asn in single BRICHOS domains. **(g)** Family and species distributions of  
1068 cases that contain Asn in multiple BRICHOS domains. **(h)** pH-dependent structural changes  
1069 of rh proSP-C BRICHOS variants monitored by CD, the details are shown in  
1070 **Supplementary Figure 5b and c.** **(i)** pH-dependent transition of rh Bri2 BRICHOS  
1071 monomers to dimers measured by Trp fluorescence, the details are shown in **Supplementary**  
1072 **Figure 9b and c.**

1073

1074



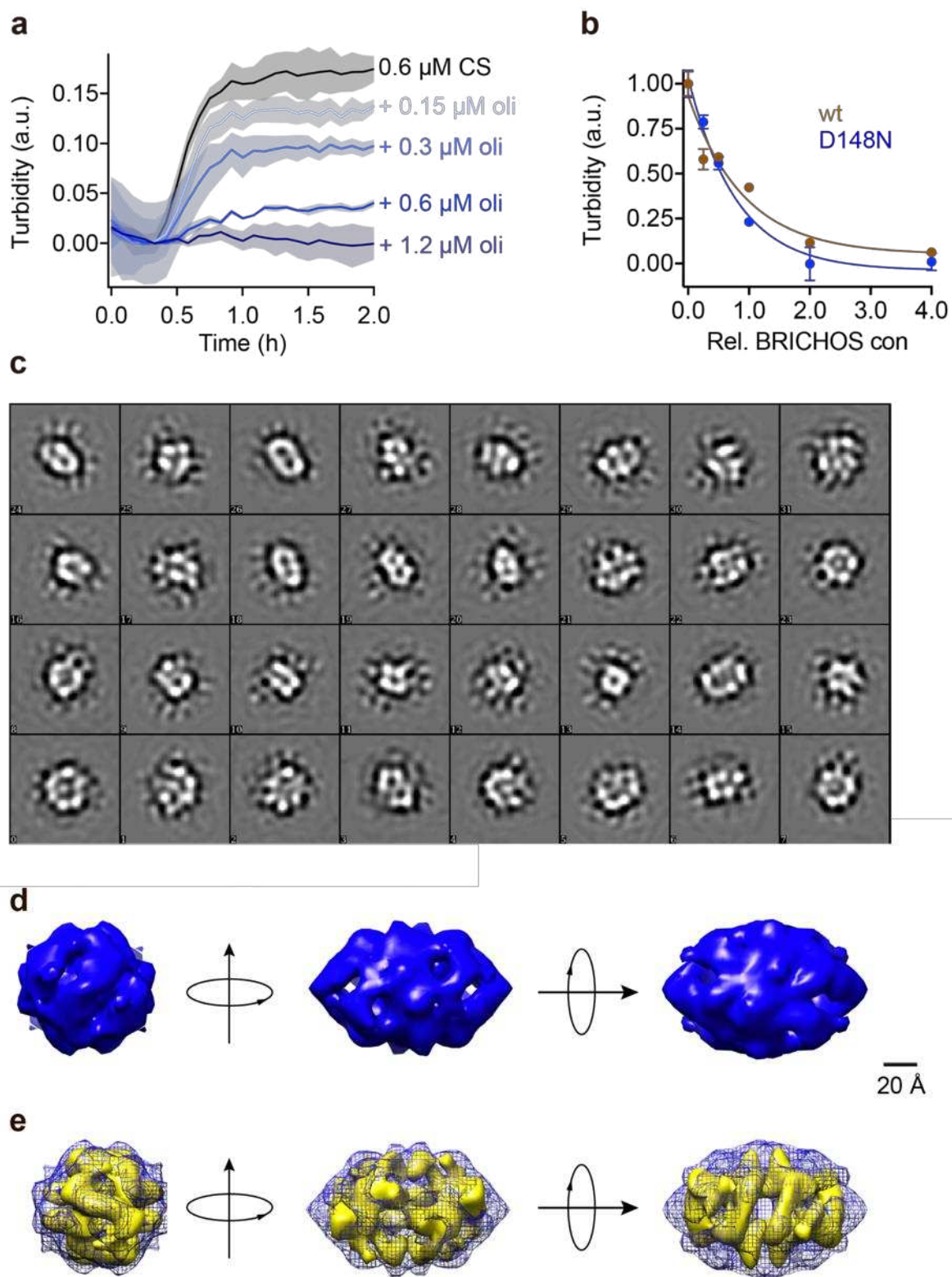
1075  
1076 **Fig. 3. Asp to Asn mutation reduces rh proSP-C BRICHOS and rh Bri2 BRICHOS**  
1077 **capacity against Aβ42 neurotoxicity.** (a) Schematic diagram of electrophysiological  
1078 recordings. The hippocampal slices from wildtype C57BL/6 mice were preincubated either  
1079 with 50 nmol L<sup>-1</sup> Aβ42 alone or co-incubated with 100 nmol L<sup>-1</sup> rh BRICHOS, and γ  
1080 oscillations were then recorded in the CA3 area. (b) Summary plot of normalized γ  
1081 oscillation power under control conditions (gray, n=20), after 15 min incubation with 50

1082 nmol L<sup>-1</sup> A $\beta$ 42 (black, n=14), 50 nmol L<sup>-1</sup> A $\beta$ 42 + 100 nmol L<sup>-1</sup> D105N (red, n=9) or  
1083 wildtype (purple, n=9) rh proSP-C BRICHOS. Example traces and example power spectra  
1084 are shown with the same color coding in (c). (d) Summary plot of  $\gamma$  oscillation power under  
1085 control conditions (gray, n=20), after 15 min incubation with 50 nmol L<sup>-1</sup> A $\beta$ 42 (black, n=14),  
1086 50 nmol L<sup>-1</sup> A $\beta$ 42 + 100 nmol L<sup>-1</sup> D148N monomeric (blue, n=11) or wildtype monomeric  
1087 (yellow, n=8) rh Bri2 BRICHOS. Example traces and example power spectra are shown with  
1088 the same color coding in (e). The data are reported as means  $\pm$  standard errors of the means.  
1089 ns, no significant difference, \*p < 0.05, \*\*p < 0.01, \*\*\*p < 0.001.

1090

1091

1092

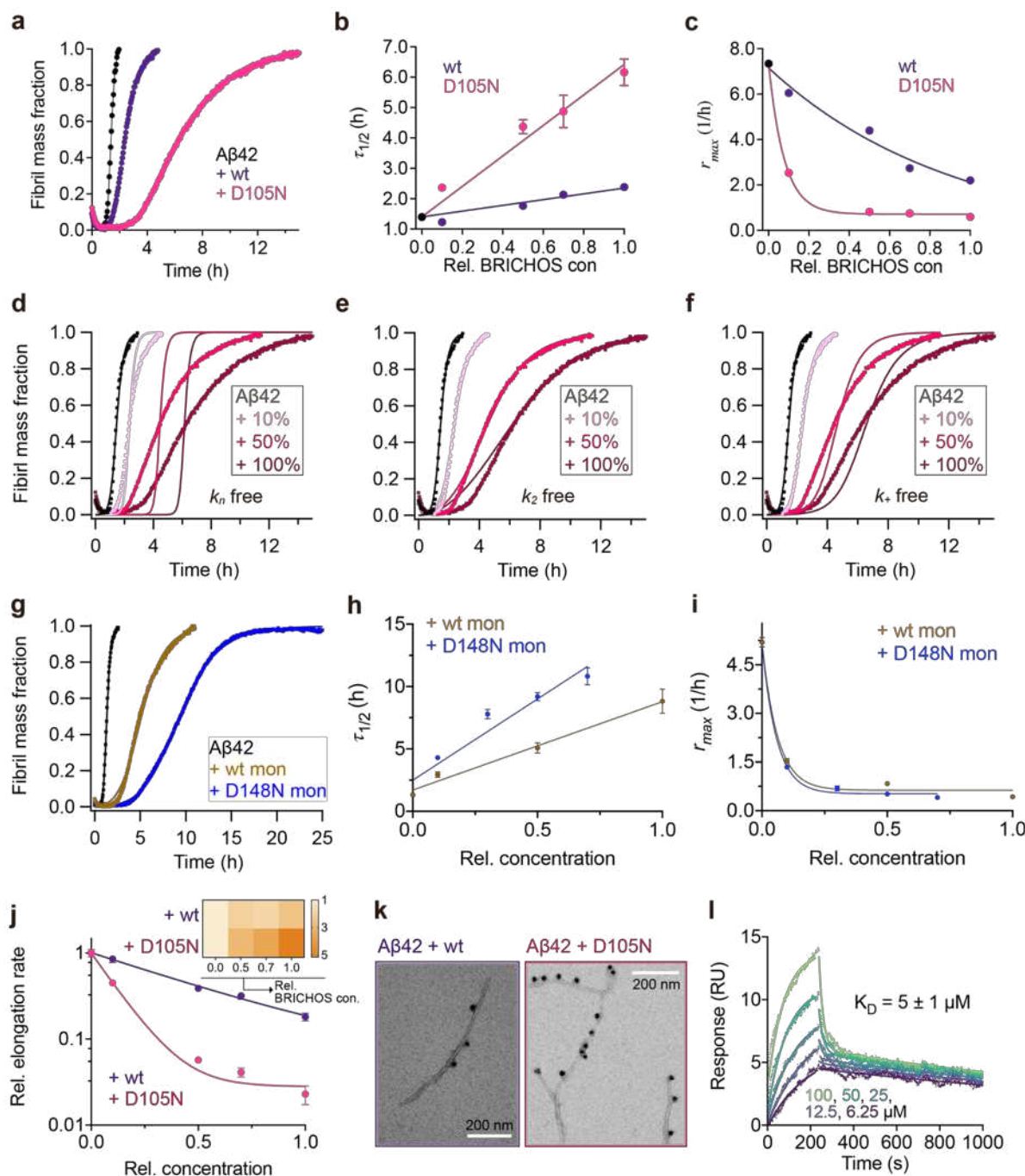


1093

1094 **Fig. 4. Rh Bri2 BRICHOS D148N oligomer EM map and comparison with the wildtype**  
1095 **oligomer 3D EM density map.** (a) Kinetics of aggregation of 600 nmol L<sup>-1</sup> citrate synthase  
1096 (CS) at 45 °C alone (black), in the presence of 0.15, 0.3, 0.6 and 1.2  $\mu\text{mol L}^{-1}$  rh Bri2  
1097 BRICHOS D148N oligomer. The different concentrations of the oligomers are shown with a  
1098 blue gradient, which are labelled on the right of the traces. (b) Effects of rh Bri2 BRICHOS

1099 D148N and wildtype oligomers (data from ref <sup>(32)</sup>) on CS aggregation at different molar ratios  
1100 (referred to monomeric subunits) of BRICHOS:CS. The data are presented as means ±  
1101 standard deviations. **(c)** 2D classes of rh Bri2 BRICHOS D148N oligomers. Most class  
1102 averages show an approximate 2-fold symmetry. **(d)** The three viewing directions are along  
1103 the three different 2-fold axes (upper panel). The map of rh Bri2 BRICHOS D148N oligomer  
1104 was based on 10 223 particles manually extracted from images recorded on a CCD detector  
1105 with ×85 200 magnification and the voxel size of the map is 2.464 Å. The lower panel shows  
1106 the 3D density map of rh Bri2 BRICHOS D148N oligomer with D2 symmetry (blue) and the  
1107 volume fit in rh wildtype Bri2 BRICHOS oligomer (yellow, EMDB: 3918).

1108



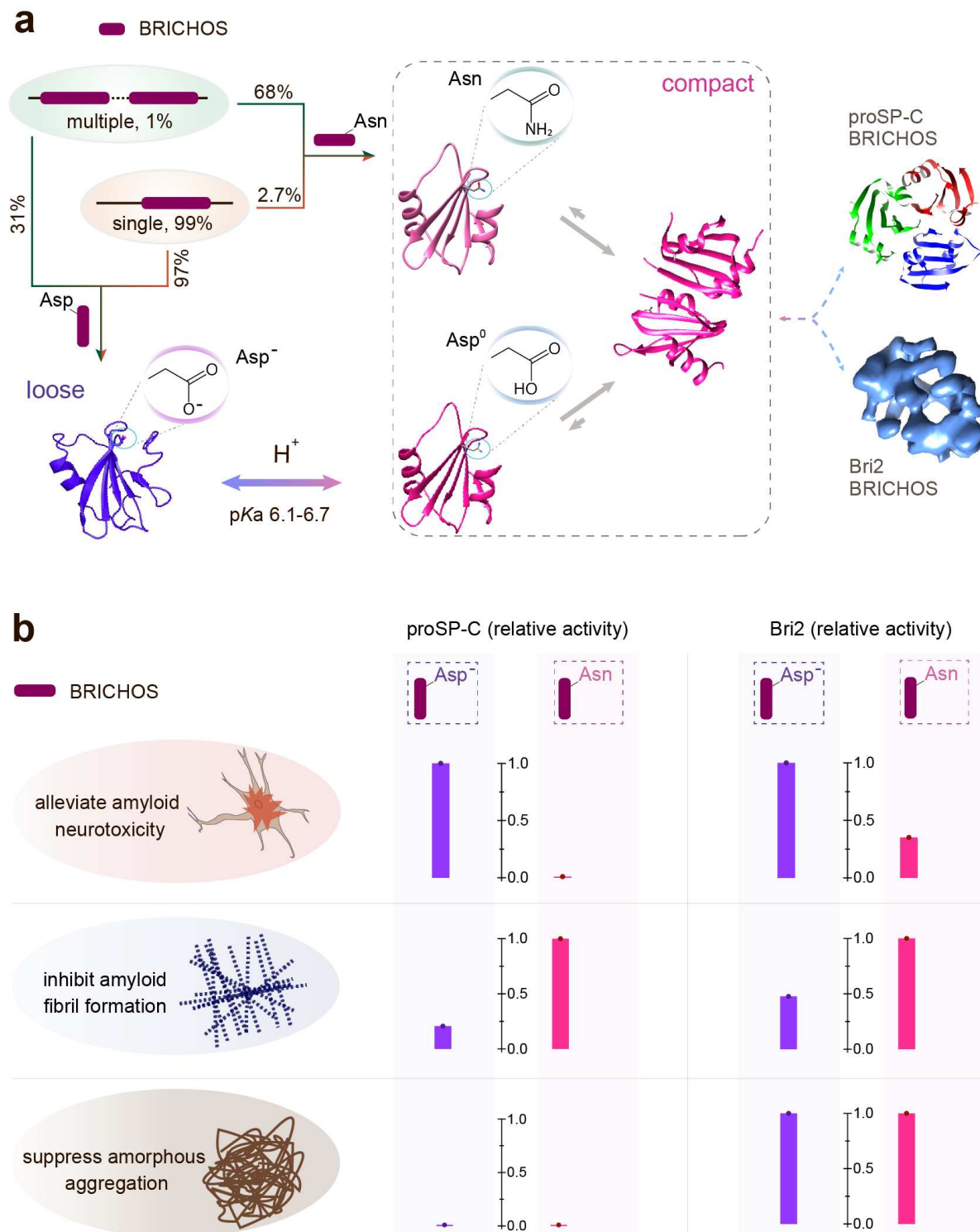
1109

1110 **Fig. 5. Asp to Asn mutation changes rh proSP-C BRICHOS activity against A $\beta$ 42 fibril**  
 1111 **formation.** (a) Activity comparison of 100% rh wildtype proSP-C BRICHOS (purple) and rh  
 1112 proSP-C BRICHOS D105N (red) against 3  $\mu\text{mol L}^{-1}$  A $\beta$ 42 (black). Individual fits with  
 1113 combined rate constants  $\sqrt{k_n k_+}$  and  $\sqrt{k_+ k_2}$  as free fitting parameters of normalized and  
 1114 averaged aggregation traces (dots) are shown as solid lines. Values for  $\tau_{1/2}$  (b) and  $r_{max}$  (c)  
 1115 extracted from sigmoidal fitting of A $\beta$ 42 aggregation traces in the presence of different  
 1116 concentrations of rh wildtype proSP-C BRICHOS (purple) or rh proSP-C BRICHOS D105N  
 1117 (red) as shown in (d–f) and (Supplementary Figure 10a–c). (d–e) Aggregation kinetics of 3

1118  $\mu\text{mol L}^{-1}$  A $\beta$ 42 in the presence of rh proSP-C BRICHOS D105N at concentrations: 0 (black),  
1119 10 (light red), 50 (red), or 100% (dark red) molar percentage referred to monomeric subunits  
1120 relative to A $\beta$ 42 monomer. The global fits (solid lines) of the aggregation traces (crosses)  
1121 were constrained such that only one single rate constant is the free fitting parameter,  
1122 indicated in each panel.  $\chi^2$  values describing the quality of the fits: 18 for  $k_n$  free, 0.8 for  $k_2$   
1123 free and 3.2 for  $k_+$  free. (g) Comparison of 50% rh wildtype Bri2 BRICHOS (yellow) and rh  
1124 Bri2 BRICHOS D148N (blue) activities against 3  $\mu\text{mol L}^{-1}$  A $\beta$ 42 (black). The solid lines are  
1125 from individual fits with combined rate constants  $\sqrt{k_n k_+}$  and  $\sqrt{k_+ k_2}$  as free fitting  
1126 parameters of normalized and averaged aggregation traces (dots). Values for  $\tau_{1/2}$  (h) and  $r_{max}$   
1127 (i) extracted from the sigmoidal fitting of A $\beta$ 42 aggregation traces in the presence of  
1128 different concentrations of rh wildtype Bri2 BRICHOS and the D148N mutant as shown in  
1129 (Supplementary Figure 10c–e). (j) Elongation rates ( $k_+$ ) determined from highly seeded  
1130 aggregation kinetics in Supplementary Figure 10d and e. The inset shows the amount of  
1131 toxic A $\beta$ 42 oligomers calculated with the relative elongation rates ( $k_+$ ) and secondary  
1132 nucleation rates ( $k_2$ ) for either rh wildtype proSP-C BRICHOS or the D105N mutant. (k)  
1133 Immuno-EM of BRICHOS bound to A $\beta$ 42 fibrils. A $\beta$ 42 was incubated with and without 100%  
1134 molar ratio of rh wildtype proSP-C BRICHOS and the D105N mutant, respectively,  
1135 overnight at 37°C. The samples were treated with a polyclonal antibody against human  
1136 proSP-C and a gold-labelled secondary antibody, and characterized by TEM. The scale bars  
1137 are 200 nm. (l) SPR sensorgrams of different concentrations (*i.e.*, 6.25, 12.5, 25, 50, and 100  
1138  $\mu\text{mol L}^{-1}$ ) of rh proSP-C BRICHOS D105N interacting with immobilized A $\beta$ 42 monomers.  
1139 The data were globally fitted for the association and disassociation phases, respectively, and  
1140 the apparent  $K_D$  was calculated.

1141

1142



1143

1144 **Fig. 6. Schematic summary of BRICHOS activities depending on ionization state of its**  
 1145 **conserved Asp.** (a) Asp and Asn in BRICHOS domains (single and multiple BRICHOS  
 1146 precursors account for 94% and 5%, and adopt “loose” and “compact” conformation,  
 1147 respectively. At neutral pH, the conserved Asp is ionized (Asp<sup>-</sup>) and BRICHOS presents an  
 1148 open structure (from ref<sup>(16)</sup>). At pH 6-7, the Asp is protonated and BRICHOS is more  
 1149 compact (PDB accession number 2YAD, from crystals prepared at pH 6.5<sup>(ref(16))</sup>) and prone to

1150 dimerize, which could be mimicked by Asn present in some BRICHOS families. Eventually,  
1151 proSP-C BRICHOS forms trimers (2YAD), while Bri2 BRICHOS forms larger oligomeric  
1152 assemblies (EMD-3918). **(b)** The activities of BRICHOS are regulated by the conserved Asp;  
1153 with its ionization form BRICHOS can efficiently present anti-amyloid-induced neurotoxicity.  
1154 Protonation of the Asp or replaced by Asn diminishes the activity for BRICHOS anti-  
1155 amyloid-induced neurotoxicity, but oppositely, the capacity inhibiting amyloid fibril is  
1156 significantly enhanced. After forming large oligomers, the general chaperone activity against  
1157 amorphous aggregation is not obviously affected. The y-axis is the normalized activity with  
1158 substrate alone as 0 and the higher activity from the wildtype species or the mutant as 1. For  
1159 the neurotoxicity, the data used are from a ratio of 1:2 (substrate: BRICHOS) for proSP-C  
1160 BRICHOS and 1:1 for Bri2 BRICHOS. For the activity against amyloid fibril formation, the  
1161 data are from a ratio of 1:1 (substrate: BRICHOS) for proSP-C BRICHOS and 1:0.5 for Bri2  
1162 BRICHOS. For the general chaperone activity against amorphous aggregation, the data used  
1163 are from a ratio of 1:2.4 (substrate: BRICHOS), both for proSP-C BRICHOS and for Bri2  
1164 BRICHOS.

1165

1166

1167

1168

1169

1170

1171

1172

1173

1174

1175

1176

1177

1178

1179

1180

1181

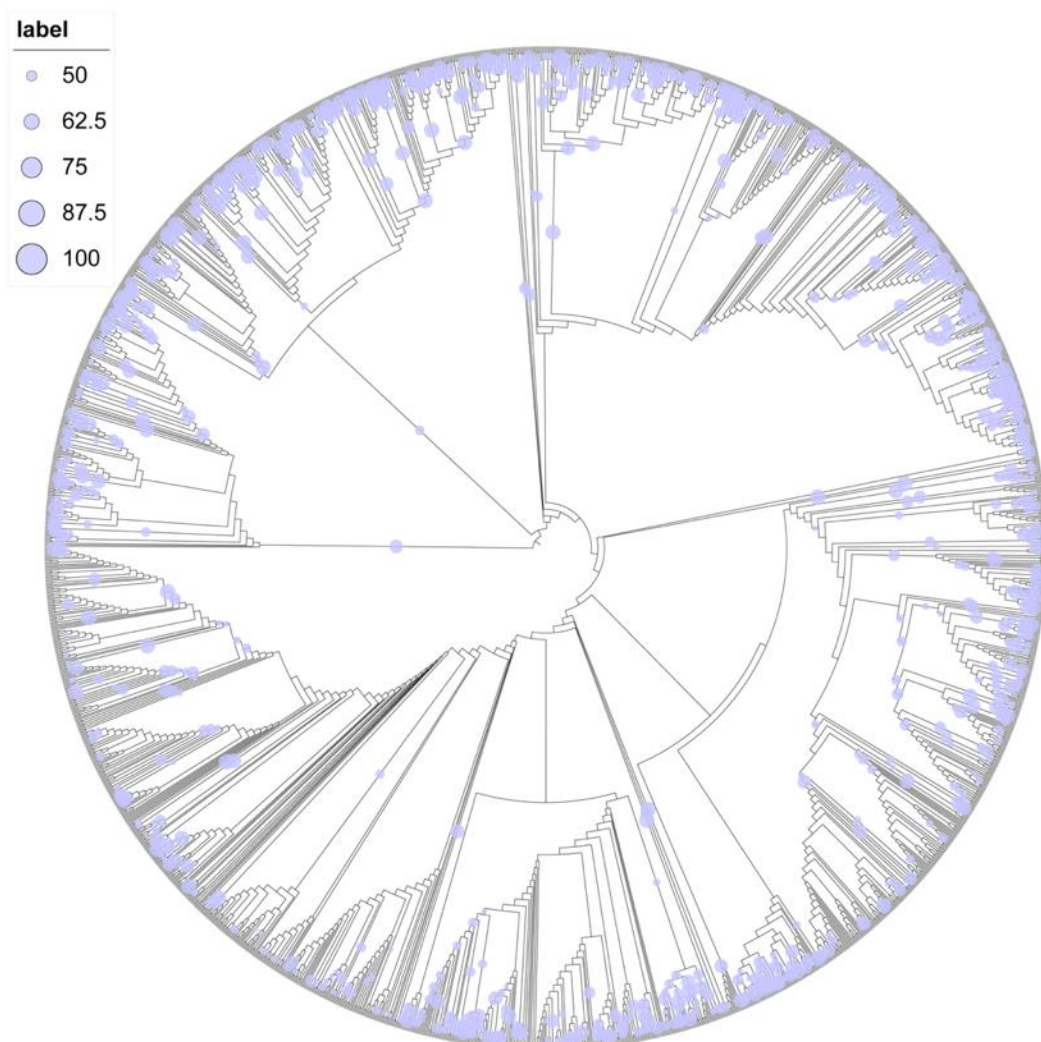
1182

1183

1184

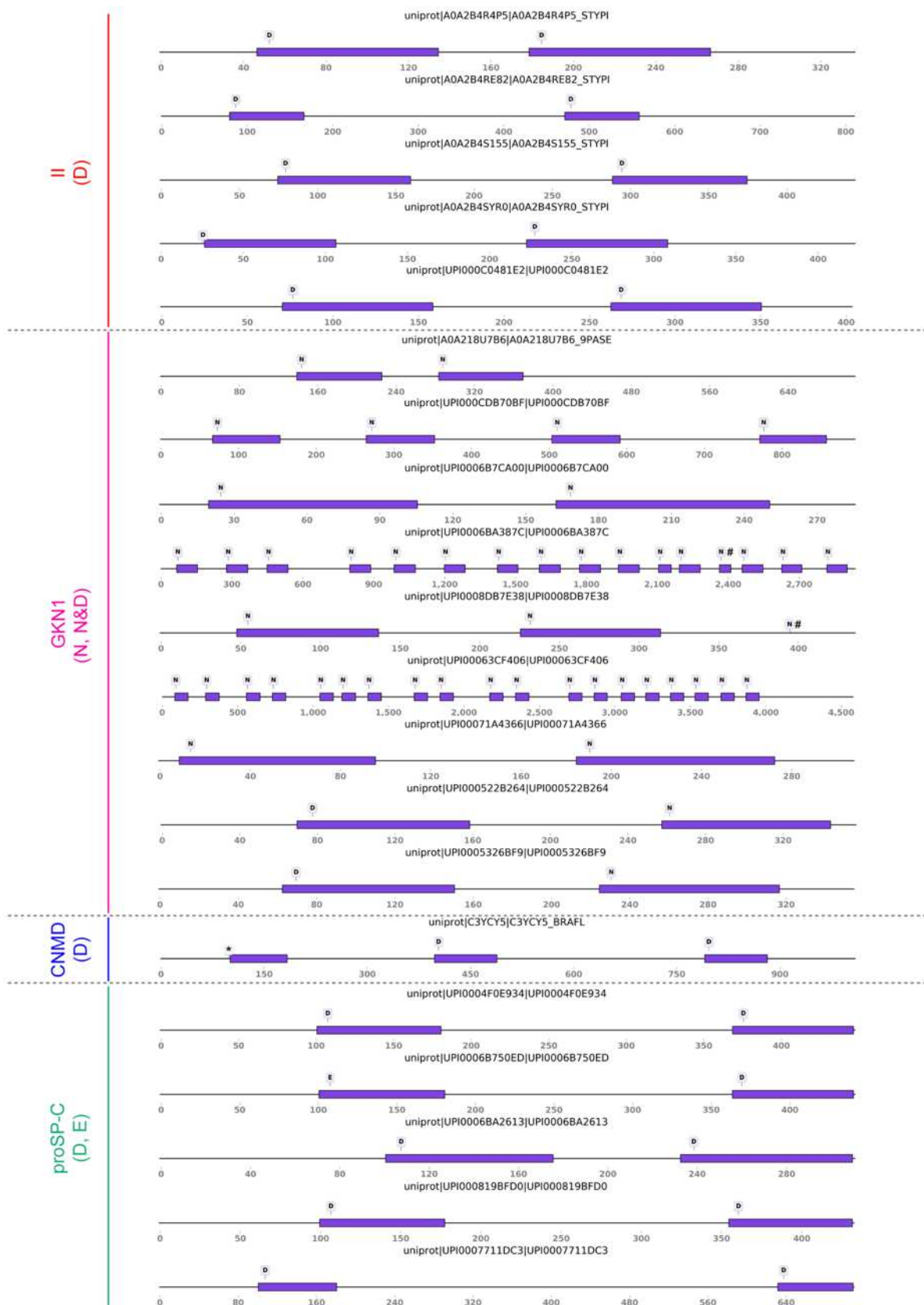
1185 **Supplementary Figures**

1186



1187

1188 **Fig. S1. Evolution of the molecular chaperone domain BRICHOS.** Phylogenetic tree of  
1189 the 2 019 BRICHOS domains, which was grouped into thirteen families (**Fig. 1c**). The  
1190 bootstrap values larger than 50% are indicated by labels, where the sizes are proportional to the  
1191 bootstrap values.



1192

1193

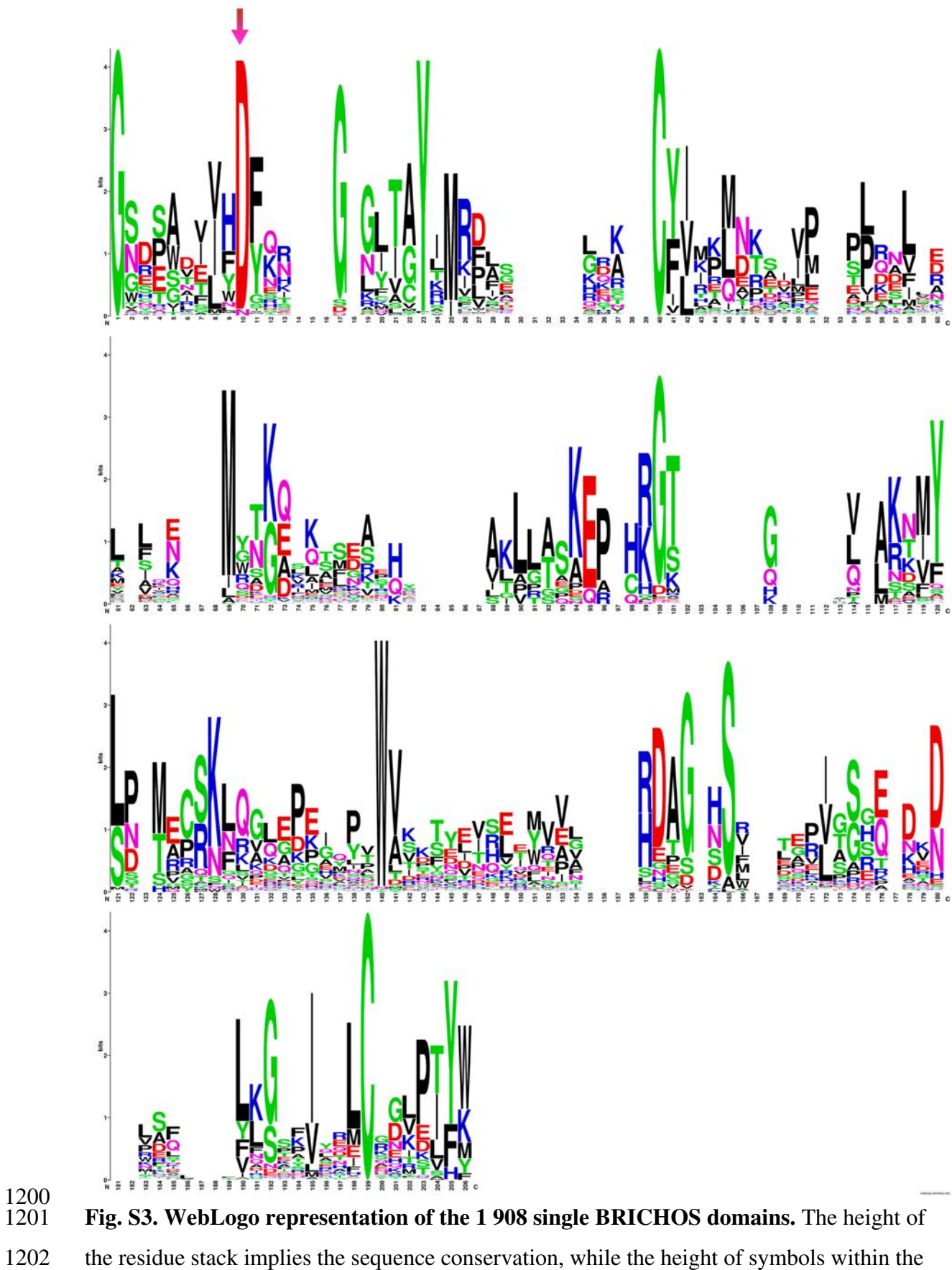
1194

1195

**Fig. S2. The architecture of proproteins containing multiple BRICHOS domains.** The proproteins contain up to nineteen multiple, tandem BRICHOS domains (multi-BRICHOS). The architecture is generally shown in **Figure 1d**. The UniProt accession number is shown

1196 over each corresponding cartoon. The length of the bar is not proportional to the size of the  
1197 BRICHOS domain from different precursors. # refers to the C-terminally truncated, and \*  
1198 indicated the N-terminally truncated.

1199

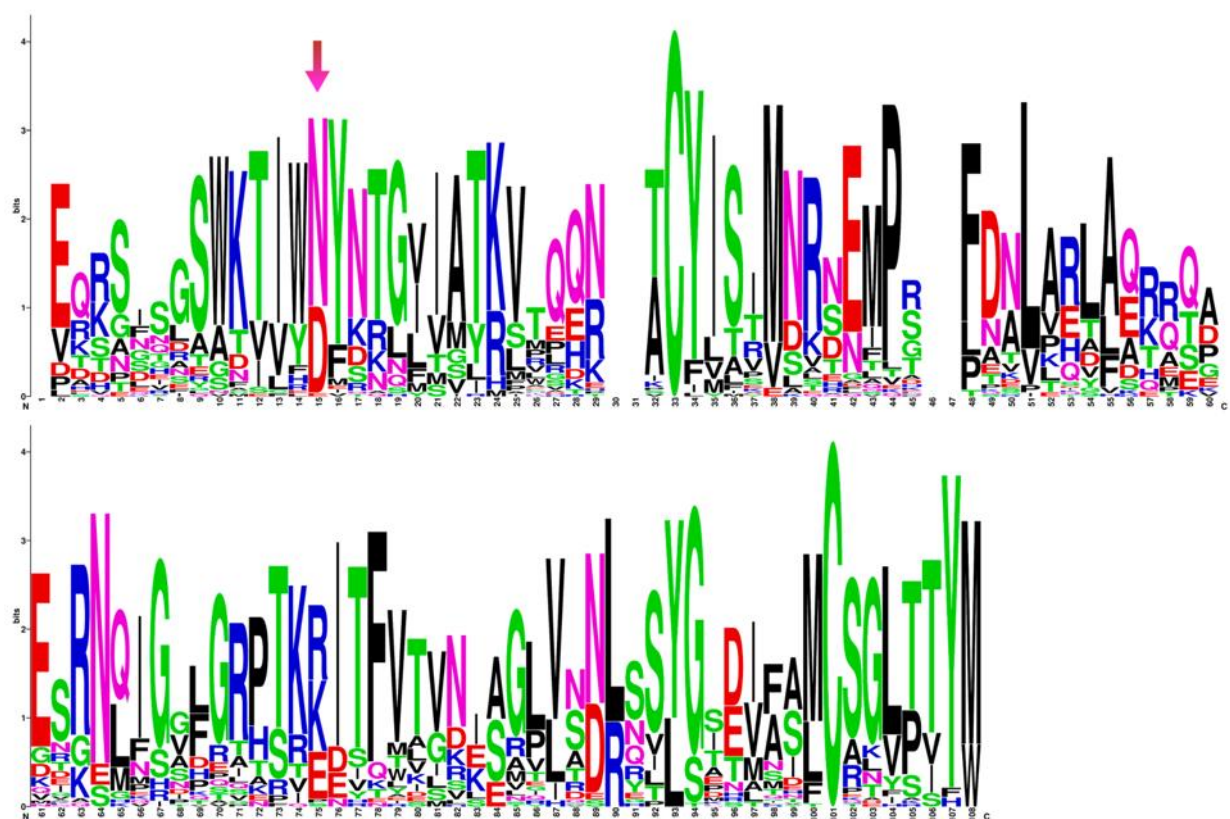


1203 stack indicates the relative frequency of each residue. The arrow marks the conserved Asp  
1204 residue.

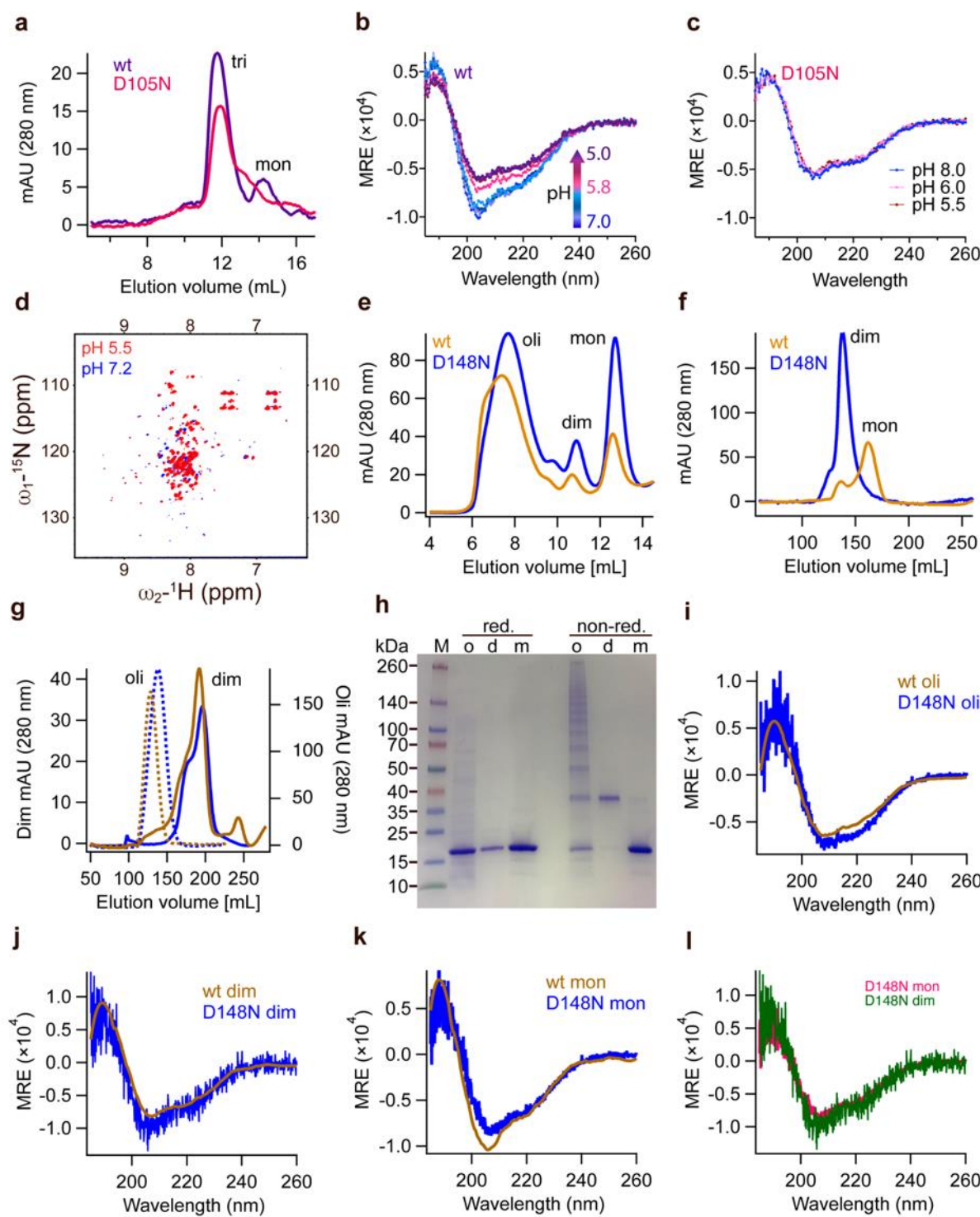
1205

1206

1207



1208  
1209 **Fig. S4. WebLogo representation of the 74 multiple BRICHOS domains.** The height of  
1210 the residue stack implies the sequence conservation, while the height of symbols within the  
1211 stack indicates the relative frequency of each residue. The arrow marks the conserved Asp  
1212 residue.



1213

1214 **Fig. S5. Characterization of rh wildtype and Asp to Asn mutant BRICHOS.** (a) SEC  
 1215 analysis of purified rh wildtype (wt) proSP-C BRICHOS (purple) and the D105N mutant  
 1216 (red). (b and c) CD measurements of rh wt proSP-C BRICHOS (purple) and the D105N  
 1217 mutant at different pHs. (d) NMR HSQC spectrum comparison of rh wt proSP-C BRICHOS  
 1218 (purple) and the D105N mutant at pH 7.2 (blue) and 5.5 (red). (e) SEC of rh wildtype (wt,  
 1219 yellow) NT\*-Bri2 BRICHOS and the D148N mutant (blue) species. oli, oligomers; dim,

1220 dimers. (f) SEC of wildtype (wt) Bri2 BRICHOS (blue) and Bri2 BRICHOS D148N (yellow)  
1221 monomer fraction prepared from corresponding fusion protein (NT\*-Bri2 BRICHOS)  
1222 monomers. dim, dimers; mon, monomers. (g) SEC of wildtype (wt) Bri2 BRICHOS (blue)  
1223 and the D148N (yellow) oligomer (dash line) and dimer (solid line) fractions prepared from  
1224 corresponding fusion protein (NT\*-Bri2 BRICHOS) oligomer and dimer. oli, oligomers; dim,  
1225 dimers. (h) SDS-PAGE analyses of SEC isolated rh Bri2 BRICHOS D148N species under  
1226 reducing and non-reducing conditions. (i-l) CD spectra of rh Bri2 BRICHOS D148N  
1227 monomers, dimers and oligomers and the comparison with rh wildtype (wt) Bri2 BRICHOS  
1228 monomer. MRE is the mean molar residual ellipticity in deg·cm<sup>2</sup>·dmol<sup>-1</sup>.

1229

1230

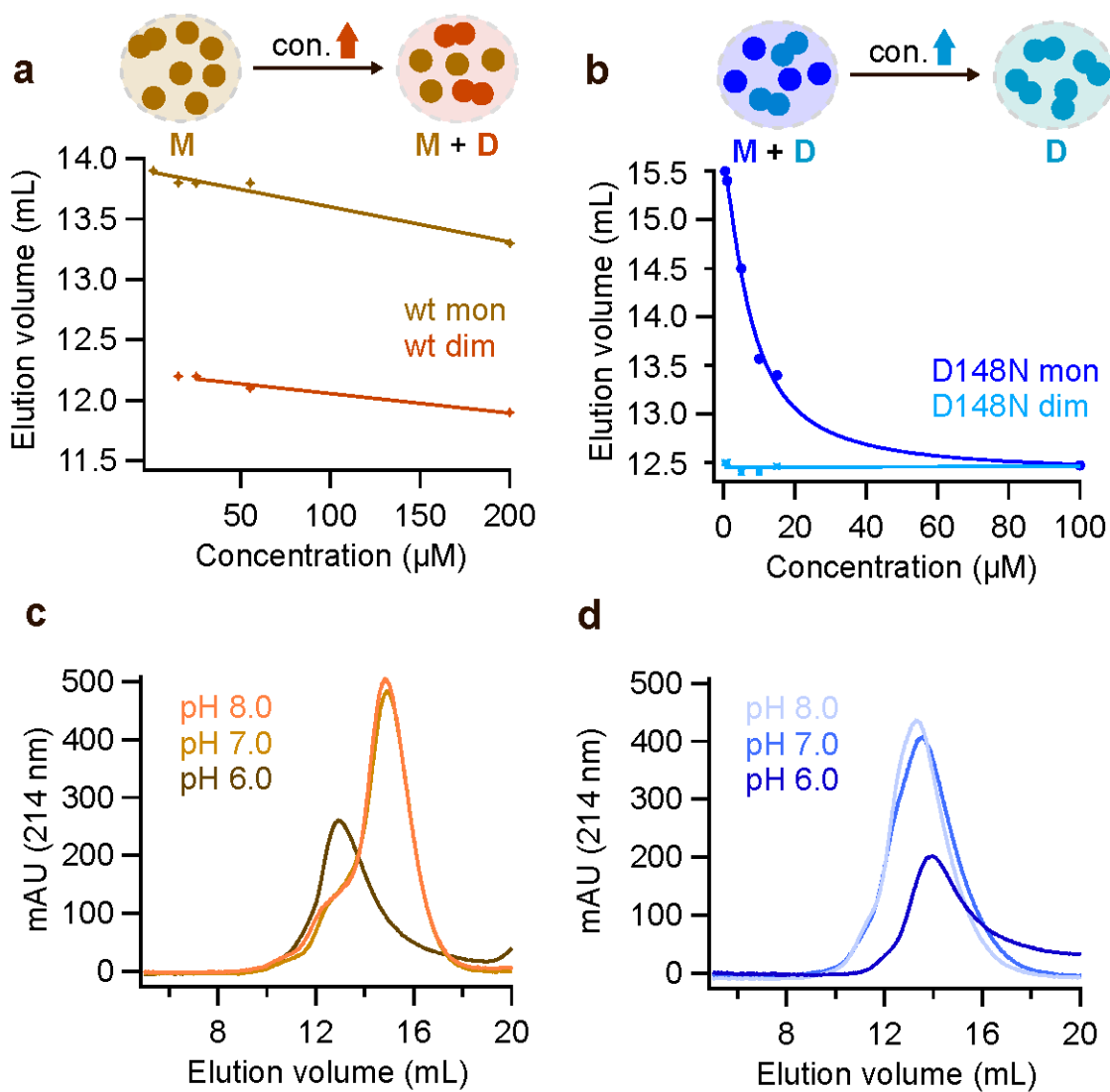
1231

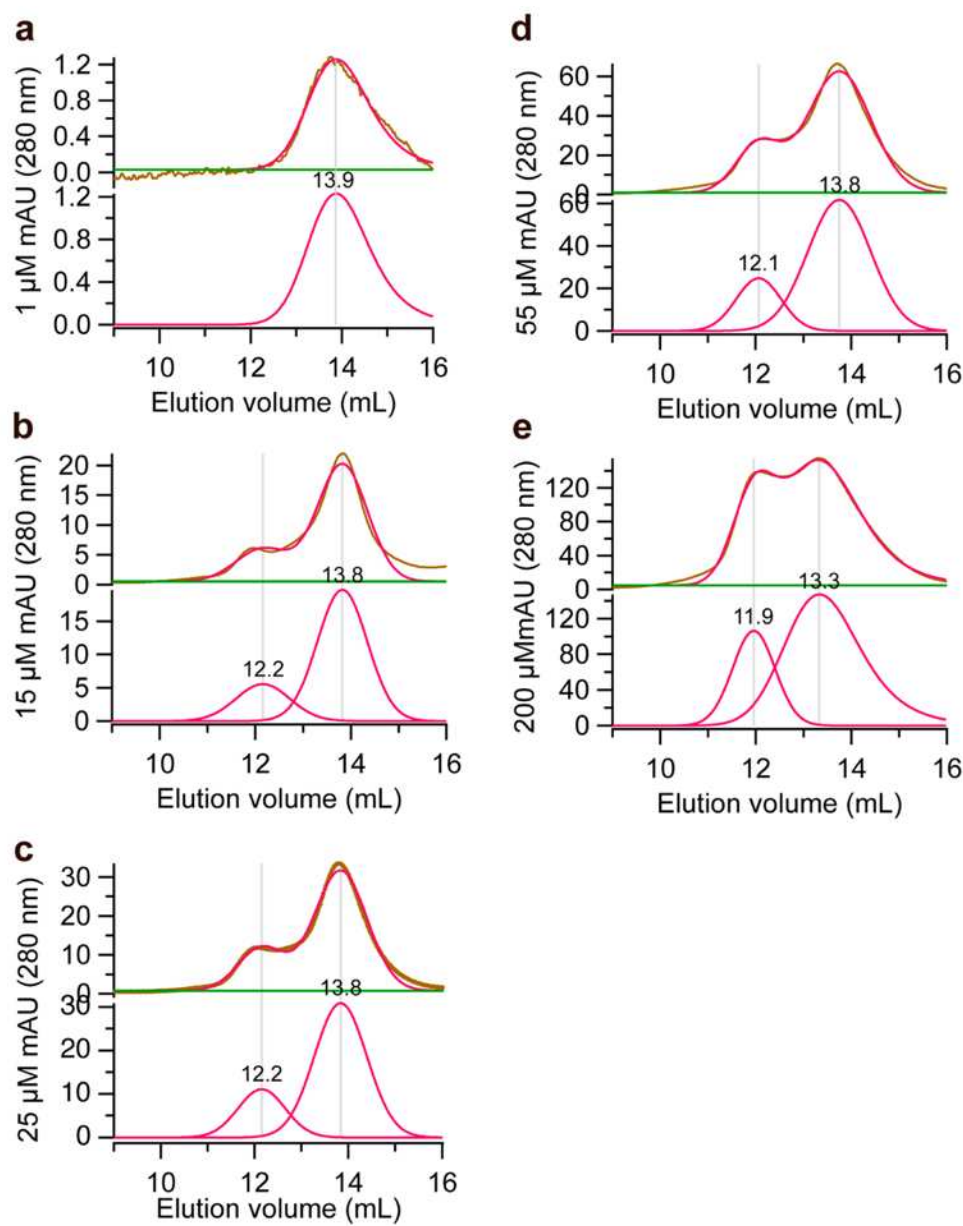
1232

1233

1234

1235

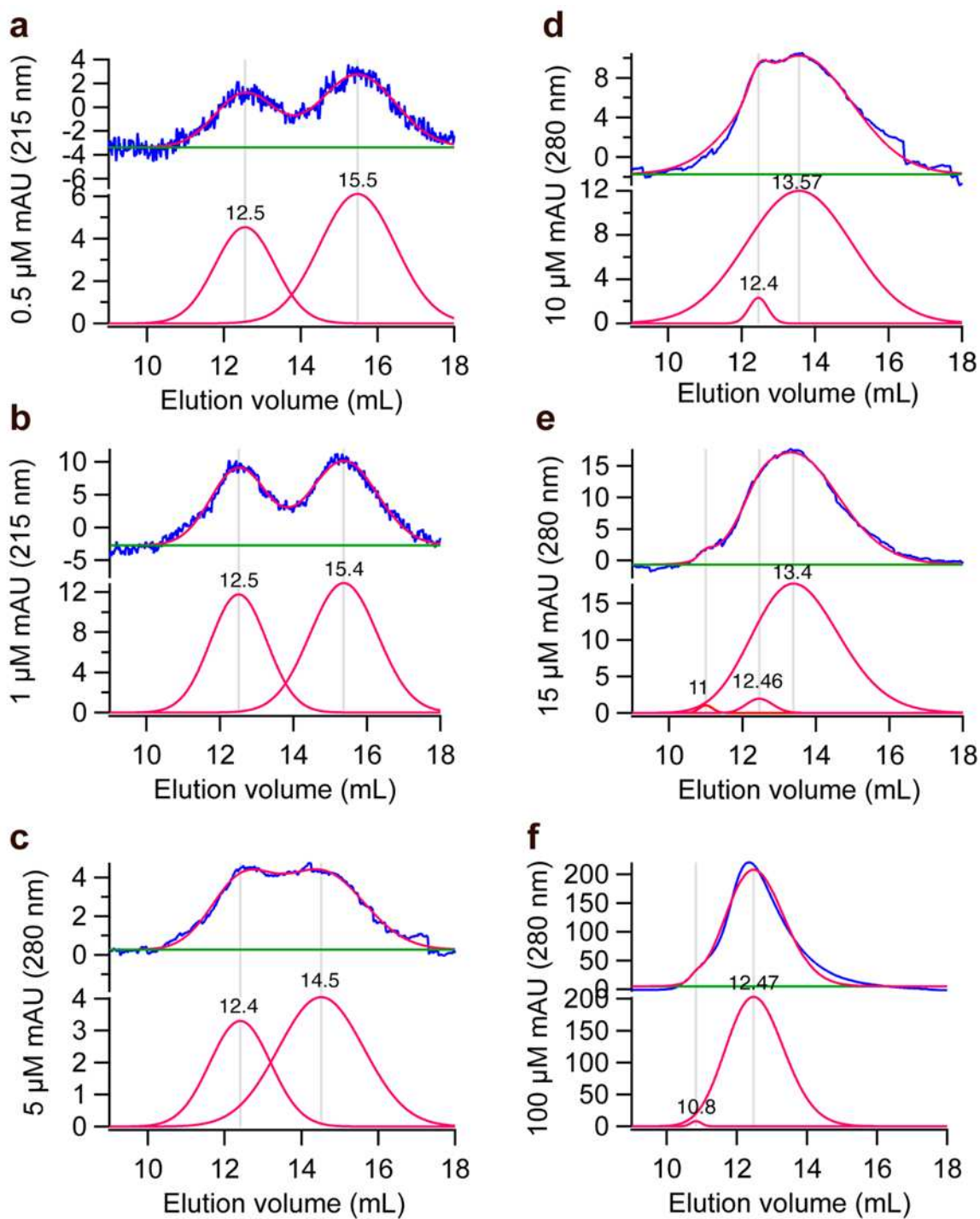




1249

1250 **Fig. S7. Rh wildtype Bri2 BRICHOS monomer concentration-dependent dimerization.**

1251 SEC analysis of rh wildtype Bri2 BRICHOS monomer at concentrations of 1 (a), 15 (b), 25  
1252 (c), 55 (d) and 200  $\mu\text{mol L}^{-1}$  (e). The top panel of each sub-figure is the raw SEC data  
1253 (yellow) with gaussian fitted (red). The lower panel of each sub-figure is the multiple  
1254 gaussian peak fitting (red) and the number on the top of each peak represents the elution  
1255 volume.



1256

1257 **Fig. S8. Rh Bri2 BRICHOS D148N monomer concentration-dependent dimerization.**

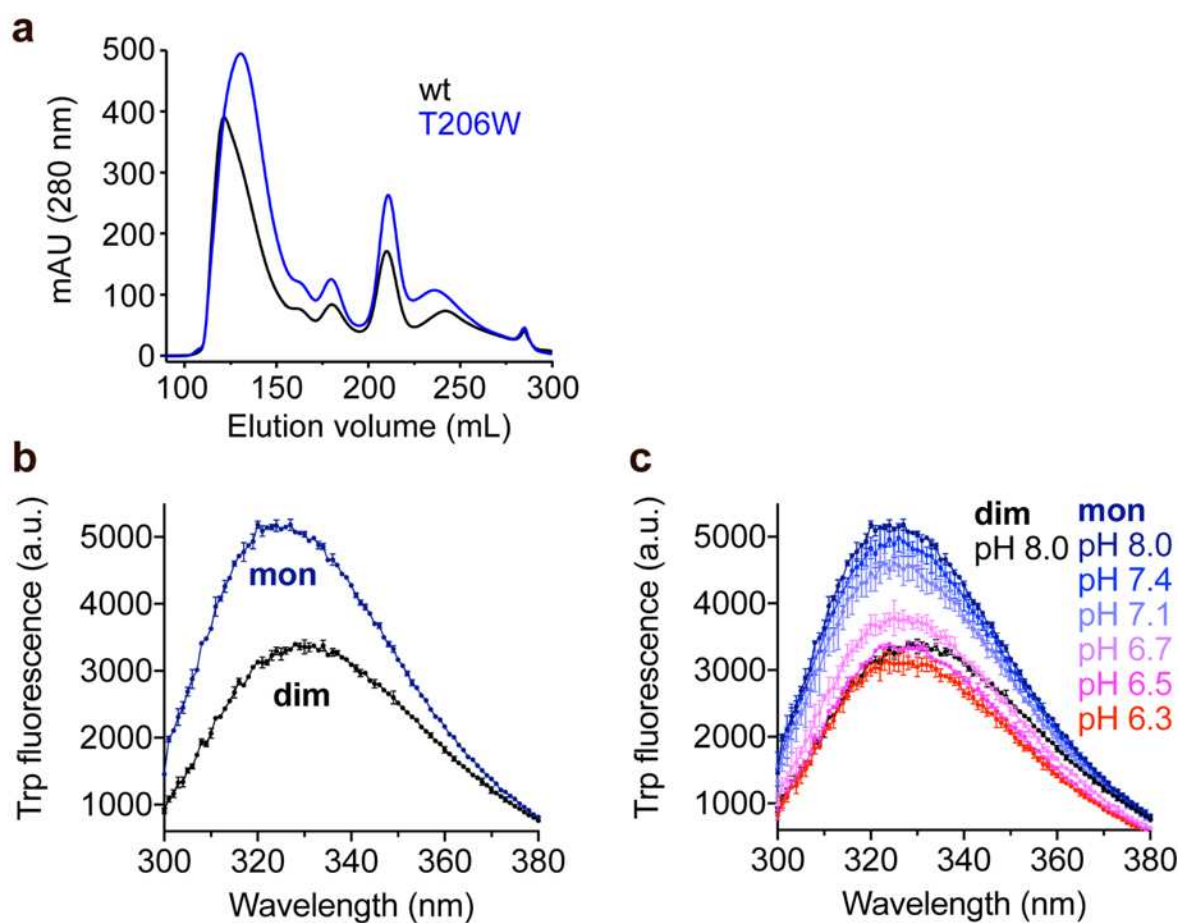
1258 SEC analysis of rh Bri2 BRICHOS D148N monomer at concentrations of 0.5 (a), 1 (b), 5 (c),  
1259 10 (d), 15(e) and 100  $\mu\text{mol L}^{-1}$  (f). The top panel of each sub-figure is the unprocessed data  
1260 (yellow) with gaussian fitted (red). The lower panel of each sub-figure is the gaussian peak  
1261 fitting (red) and the number on the top of each is the relevant elution volume.

1262

1263

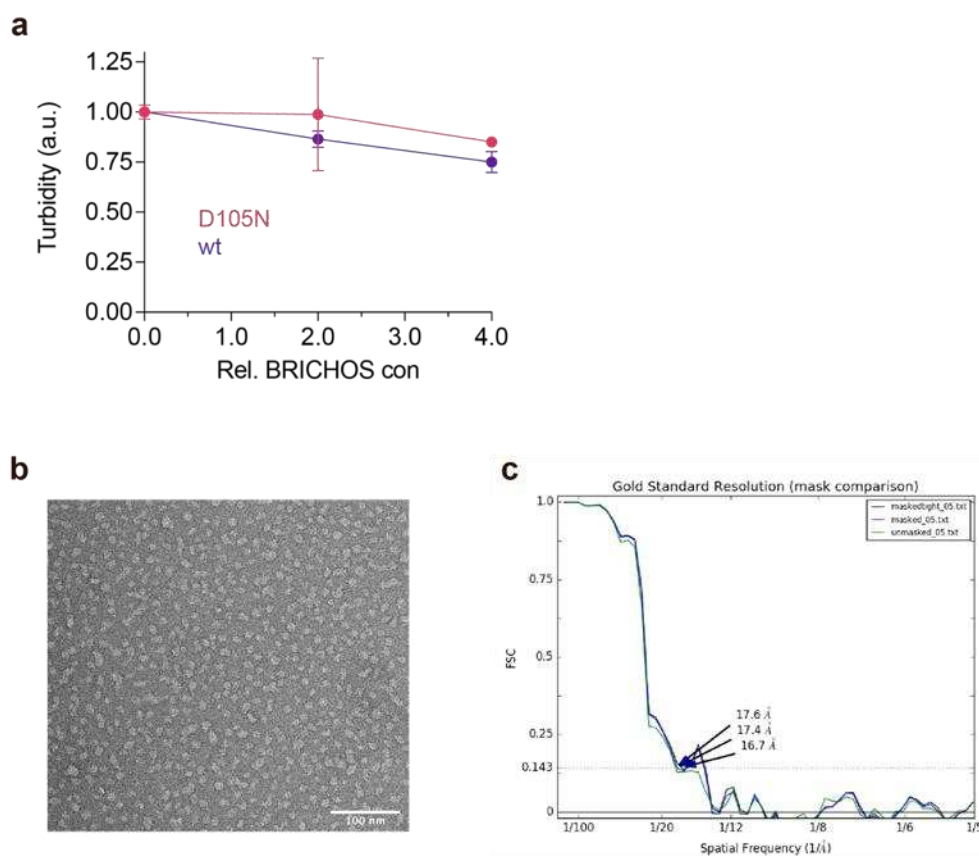
1264

1265



1266

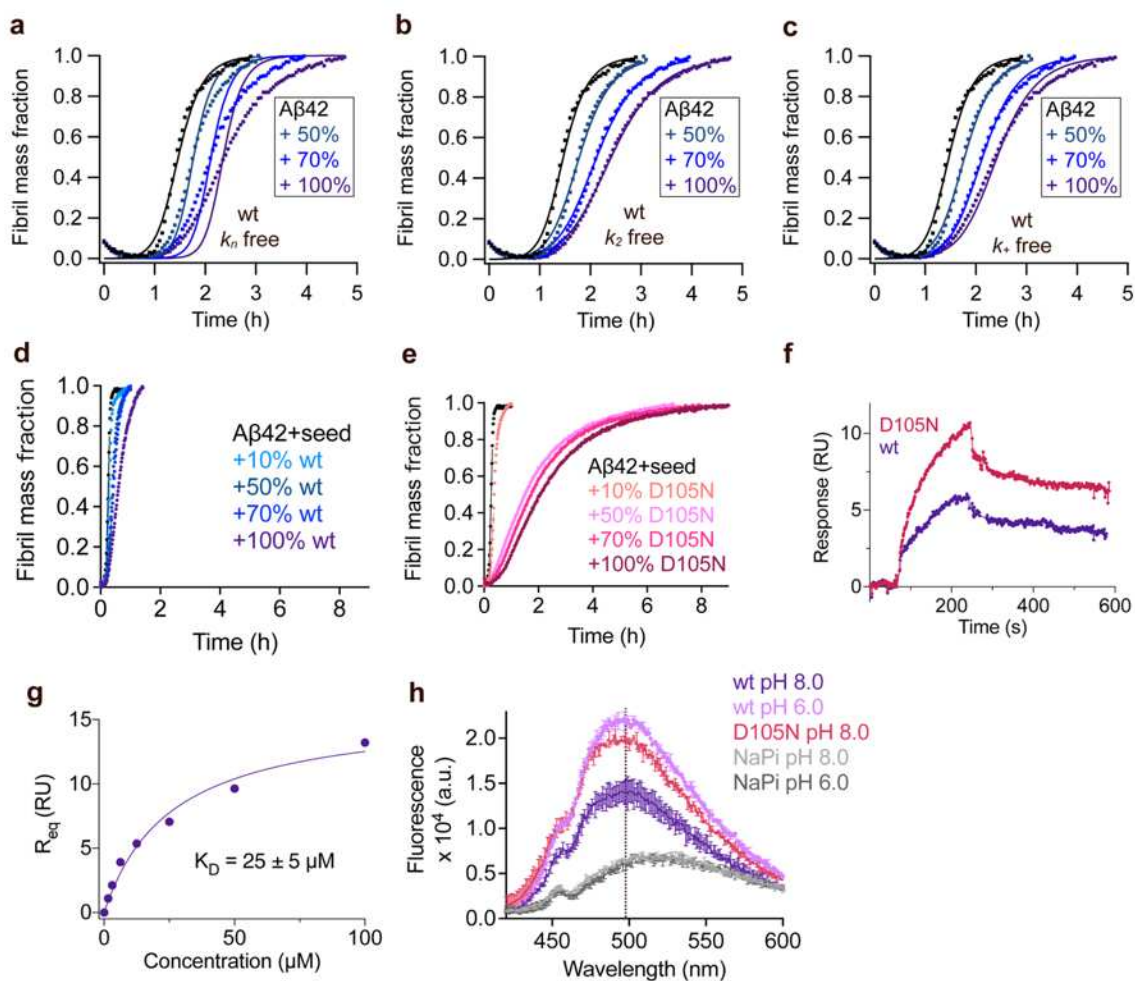
1267 **Fig. S9. Trp fluorescence of rh Bri2 BRICHOS T206W mutant.** (a) SEC of rh wildtype  
1268 NT\*-Bri2 BRICHOS and the rh NT\*-Bri2 BRICHOS T206W mutant. (b) Rh Bri2  
1269 BRICHOS T206W monomers and dimers were diluted to 2  $\mu\text{mol L}^{-1}$  in 20  $\text{mmol L}^{-1}$  NaPi,  
1270 0.2  $\text{mmol L}^{-1}$  EDTA at pH 8.0. (b) Rh Bri2 BRICHOS T206W monomers at different pHs  
1271 from pH 6.3 to pH 8.0 were subjected to Trp fluorescence measurements, while the dimers  
1272 were measured at pH 8.0. All the samples were prepared in duplicates, and excited at 280 nm  
1273 (5  $\mu\text{m}$  bandwidth) and fluorescence emission from 300–400 nm (10  $\mu\text{m}$  bandwidth, 1 nm step  
1274 interval) was recorded. For the final fluorescence intensities, the results were corrected by  
1275 subtracting the background fluorescence. The data are presented as means  $\pm$  standard  
1276 deviations.



1277

1278 **Fig. S10. Electron microscopy analyses of rh Bri2 BRICHOS D148N oligomers. (a)**  
1279 Effects of rh proSP-C BRICHOS variants on CS aggregation at different molar ratios of  
1280 BRICHOS:CS. The data are presented as means  $\pm$  standard deviations. **(b)** Raw TEM  
1281 micrograph of negatively stained rh Bri2 BRICHOS D148N oligomers. **(c)** The Fourier shell  
1282 correlation (FSC) indicates a resolution of  $\sim$ 17 Å for the reconstructed 3D density map  
1283 determined at an FSC-value of 0.143 (dotted lines).

1284



1285

1286 **Fig. S11. Rh wildtype proSP-C BRICHOS interferes with A $\beta$ 42 fibril formation. (a-c)**  
1287 Aggregation kinetics of 3  $\mu$ mol L $^{-1}$  A $\beta$ 42 in the presence of rh wildtype (wt) proSP-C  
1288 BRICHOS at concentrations: 0 (black), 50 (cyan), 70 (blue), or 100% (purple) molar  
1289 percentage referred to monomeric subunits relative to A $\beta$ 42 monomer concentration. The  
1290 global fits (solid lines) of the aggregation traces (cross) were constrained such that only one  
1291 single rate constant is the free fitting parameter. (d and e) Seeded aggregation traces of 3  
1292  $\mu$ mol L $^{-1}$  A $\beta$ 42 with 0.6  $\mu$ mol L $^{-1}$  preformed A $\beta$ 42 fibril seeds in the presence of different  
1293 concentration of rh wildtype proSP-C BRICHOS (d) and the D105N mutant (e). (f) Analysis  
1294 of rh wildtype (wt) proSP-C BRICHOS (purple) and the D105N mutant (red) binding to  
1295 A $\beta$ 42 monomers detected by SPR. 25  $\mu$ mol L $^{-1}$  rh wildtype proSP-C BRICHOS and the  
1296 D105N mutant were injected in over the chip surfaces, respectively. The response from the  
1297 blank surface was subtracted from the immobilized surface response. (g) Steady state affinity  
1298 for rh proSP-C BRICHOS D105N to immobilised A $\beta$ 42 monomers. Different concentrations  
1299 of rh proSP-C BRICHOS D105N mutant, *i.e.* 0, 1.56, 3.13, 6.25, 12.5, 25, 50 and 100  $\mu$ mol  
1300 L $^{-1}$ , were individually injected over the chip surfaces. Steady state affinity was estimated by

1301 plotting the maximum binding responses versus BRICHOS concentrations. (h) Fluorescence  
1302 emission of 2  $\mu\text{mol L}^{-1}$  bis-ASN in sodium phosphate buffer at pH 8.0 (gray) or 6.0 (black) or  
1303 in the presence of 1  $\mu\text{mol L}^{-1}$  rh wildtype proSP-C BRICHOS at pH 8.0 or 6.0 and the  
1304 D105N mutant.

1305

1306

1307

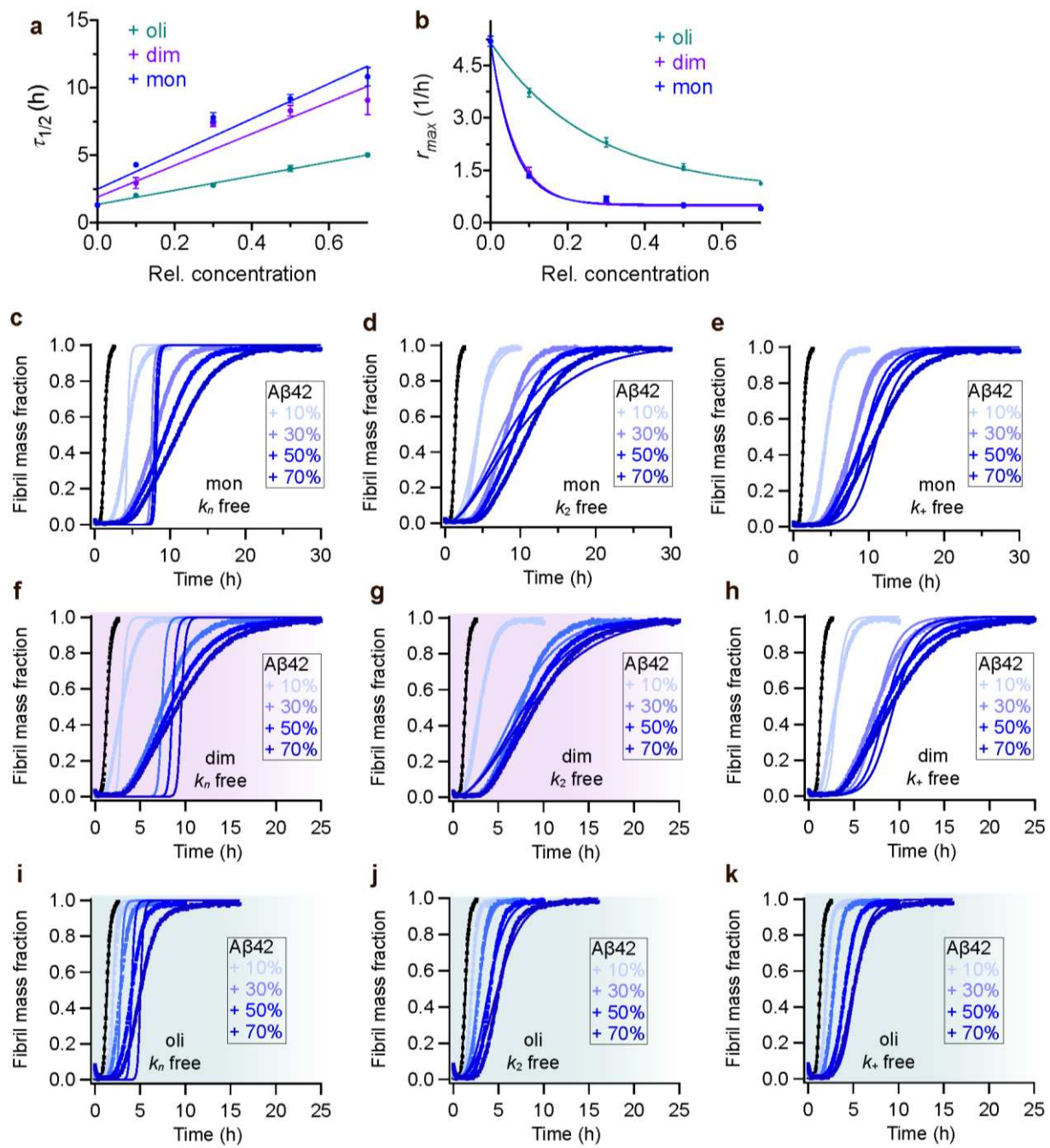
1308

1309

1310

1311

1312



1313

1314

**Fig. S12. Rh Bri2 BRICHOS D148N inhibition of A $\beta$ 42 fibril formation.** Values for  $\tau_{1/2}$

1315 (a) and  $r_{max}$  (b) extracted from the sigmoidal fitting of A $\beta$ 42 aggregation traces in the

1316 presence of different concentrations of rh Bri2 BRICHOS D148N species as shown in (c–k).

1317 (c–e) Aggregation kinetics of 3  $\mu$ mol L $^{-1}$  A $\beta$ 42 in the presence of rh Bri2 BRICHOS D148N

1318 monomers at different concentrations. The global fits (solid lines) of the aggregation traces

1319 (cross) were constrained such that only one single rate constant is the free fitting parameter,

1320 indicated in each panel.  $\chi^2$  values describing the quality of the fits: 62 for  $k_n$  free, 11.2 for  $k_2$

1321 free and 3.7 for  $k_+$  free. (f–h) Aggregation kinetics of 3  $\mu$ mol L $^{-1}$  A $\beta$ 42 in the presence of rh

1322 Bri2 BRICHOS D148N dimers at different concentrations. The global fits (solid lines) of the

1323 aggregation traces (cross) were constrained such that only one single rate constant is the free  
1324 fitting parameter, indicated in each panel.  $\chi^2$  values describing the quality of the fits: 43 for  
1325  $k_n$  free, 3.9 for  $k_2$  free and 7.8 for  $k_+$  free. (i–k) Aggregation kinetics of 3  $\mu\text{mol L}^{-1}$  A $\beta$ 42 in  
1326 the presence of rh Bri2 BRICHOS D148N oligomers at different concentrations. The global  
1327 fits (solid lines) of the aggregation traces (cross) were constrained such that only one single  
1328 rate constant is the free fitting parameter.  $\chi^2$  values describing the quality of the fits: 8.6 for  
1329  $k_n$  free, 1.4 for  $k_2$  free and 0.4 for  $k_+$  free. For the different D148N species, both  $k_2$  and  $k_+$  as  
1330 sole free fitting rate, the fibrillization traces were described with similar  $\chi^2$  values,  
1331 suggesting both  $k_2$  and  $k_+$  might be affected, like the wildtype species.

1332  
1333  
1334

1335 **Supplementary Table.**

1336 **Table S1. Species distribution and pairwise alignment of the multiple BRICHOS**  
1337 **domains.** See separate file.

1338 **Table S2. Summary of statistics performed in Fig. 3b and d.**

1339

1340 **Source data:**

1341 **Figure 3-source data.**

1342 **Figure 4-source data.**

1343 **Figure 5-figure supplement 5-source data**

1344  
1345